crystals

MDPI

Review

Recent Advancements of N-Doped Graphene for Rechargeable Batteries: A Review

Rabia Ikram [1,*], Badrul Mohamed Jan [1], Syed Atif Pervez [2,3], Vassilis M. Papadakis [4], Waqas Ahmad [5], Rani Bushra [6], George Kenanakis [4] and Masud Rana [7,8]

1 Department of Chemical Engineering, University of Malaya, Kuala Lumpur 50603, Malaysia; badrules@um.edu.my
2 Helmholtz Institute Ulm, Helmholtzstraße, 11, D-89081 Ulm, Germany; syedatif.pervez@partner.kit.edu
3 Karlsruhe Institute of Technology, P.O. Box 3640, D-76021 Karlsruhe, Germany
4 Institute of Electronic Structure and Laser, Foundation for Research and Technology-Hellas, N. Plastira 100, Vasilika Vouton, GR-700 13 Heraklion, Crete, Greece; billyp@iesl.forth.gr (V.M.P.); gkenanak@iesl.forth.gr (G.K.)
5 Institute of Chemical Sciences, University of Peshawar, Peshawar 25120, Pakistan; waqasahmad@uop.edu.pk
6 Department of Chemistry, University of Malaya, Kuala Lumpur 50603, Malaysia; Bushrachem07@gmail.com
7 Materials Engineering, School of Mechanical and Mining Engineering, The University of Queensland, St Lucia, QLD 4072, Australia; m.rana@uq.edu.au
8 Redflow Sustainable Energy Storage, 27 Counihan Rd, Seventeen Mile Rocks 4073, Queensland, Australia
* Correspondence: raab@um.edu.my

Received: 6 November 2020; Accepted: 23 November 2020; Published: 26 November 2020

Abstract: Graphene, a 2D carbon structure, due to its unique materials characteristics for energy storage applications has grasped the considerable attention of scientists. The highlighted properties of this material with a mechanically robust and highly conductive nature have opened new opportunities for different energy storage systems such as Li-S (lithium-sulfur), Li-ion batteries, and metal-air batteries. It is necessary to understand the intrinsic properties of graphene materials to widen its large-scale applications in energy storage systems. In this review, different routes of graphene synthesis were investigated using chemical, thermal, plasma, and other methods along with their advantages and disadvantages. Apart from this, the applications of N-doped graphene in energy storage devices were discussed.

Keywords: N-doped graphene; synthetic routes; energy storage; Li-ion batteries; Li-sulfur batteries; graphene characterization

1. Introduction

Over the years, there is increased consumption and rapid use of fossil fuels for sustainable energy [1]. However, considering the environmental friendliness and cost, most of the research studies are targeted at production, effective conversion, and storage of renewable and sustainable energy [2]. Owing to this, the role of the energy storage system plays a vital role in different energy technologies such as electric vehicles and portable devices [3,4]. Nowadays, graphene (Gp) has gained prominence owing to its excellent electronic features and superior materials properties [5]. It is easily achievable from graphite (Gr) in a single layer sheet of sp^2 hybridized carbon atoms organized in a structure of honeycomb lattice (HL) [6,7] with exceptional characteristics that include superior electrical conductivity with exceptionally high mechanical strength, excellent chemical stability, and increased surface area [8,9].

The instantaneous developments of energy technology have been progressed for the enriched energy rechargeable batteries (ERB). Therefore, extensive research has been carried out over the last

years to improve ERB [10,11], which requires materials with excellent properties. For over two decades, various energy storage technologies such as Li-ion batteries (LIBs), Na-ion batteries (NIBs) [12,13], Zn-ion batteries (ZIBs) [14], Li-S batteries [15,16], and K-ion batteries [17] have been introduced due to their improved and high energy densities in energy technologies [18]. In battery technology, the Gp-based materials appear to be highly desirable material considering their various feasible electrical, mechanical, and physical properties [19]. Gp shows fluorescent over a wide range of wavelengths due to its heterogeneous electronic structure, flexibility, optical transparency, and high mobility for the optoelectronic devices [20]. Gp imparts an essential role in optic based devices such as optical frequency convertors, terahertz devices, optical frequency converters, and flexible smart windows [21,22]. Moreover, it has become the best alternative material used for photocatalysis treatment in which it acts as an electron scavenger, so recombination of electron-hole was remarkably decreased. Consequently, enhancing the overall efficiency of the catalyst [7,9].

Therefore, Gp has been considered as a multifaceted nanomaterial for other advanced energy-based applications such as Al-Gp ultrahigh cathode [23], Mg/Gp cathode electrode [24], SiO_x/Gp composite anode [25], Gp induced ZnO anode [26], Gp induced Li/Na anodes [27], Sn-SnSb nanoparticles induced on N-doped Gp sheets as anode [28], Gp additives on Pb-acid electrodes [29], Fl-modified Gp anode [30], and Nano-Si composite with N-doped Gp as anode [31] have been utilized in various LIBs, NIBs, and metal-air batteries. Hence, it is equally important to synthesize Gp on a large scale to quantify the demand for this material in various applications. There are extensive studies available in the literature on the Gp applications. However, this work highlights N-doped Gp synthetic routes along with their characterization techniques in the battery domain followed by their applications in rechargeable and (Li-ion, Li-S) and Metal-Air batteries. This review aims to simplify the importance of N-doped Gp in battery research to promote their future market penetration.

2. Gp Synthesis Routes for Battery Application

Gp synthesis states various methods for its fabrication depending on the desired purity, and size of the product. The first attempt of monolayer Gr synthesis was performed in early 1975 when B. Lang et al. [32] revealed the formation of Gr with mono and multilayers by using a carbon thermal decomposition process on single platinum substrates. This method continued further investigations due to the lack of uniformity of Gr layers. Furthermore, synthesis of Gp was conducted again in 2000 [33]. Though, Novoselov et al. [34] were accredited for the discovery of Gp in 2004. They have first revealed the Gp synthesis using the exfoliation process. Until now, the approach has been pursued, along with efforts to develop new techniques for efficient synthesis of large-scale development of Gp.

In the last decade, several methods were established and utilized to synthesize Gp. The most common Gp synthesis methods utilized are mechanical exfoliation (ME) [35], chemical exfoliation (CE) [36], chemical synthesis (CS) [37], electrochemical exfoliation [38], and chemical vapor deposition (CVD) process [39]. Other reported methods of Gp synthesis include the unzipping process of carbon nanotubes (UPCNTs) [40] and microwave process (MP) [41]. In ME process, the limitation of Gp layer thickness is up to 10 nm, which is 30 times thicker than the normal Gp [42]. In the CE route, solution dispersed Gr is chemically exfoliated by introducing a large number of alkali ions between the Gr layers. This process has also been applied to the graphite oxide (GrO) synthesis [43].

The thermal chemical vapor deposition (TCVD) process has demonstrated the most substantial route to produce large-scale Gp [44]. TCVD is conducted in a resistive heating furnace. Besides, plasma-enhanced chemical vapor deposition (PECVD) [45] involved methane and other gas ratios to synthesize Gp using plasma-assisted growth. These synthesis routes also exhibit some limitations depending on the properties of Gp. For example, the ME process has produced monolayer or multilayered Gp. However, the consistency of producing a similar Gp structure using this method is too difficult. Besides, the CS method is conducted in low-temperature conditions, which makes it a suitable process to synthesize Gp on multitypes of substrates at ambient temperature, specifically on the substrate made from a polymeric material. Nonetheless, Gp large areas fabricated in this

route are dispersed and nonuniform. However, Gp produced by the reduced graphene oxide (rGO) process typically leads to the incomplete GO reduction that causes a successive debasement of the electrical characteristics based on its reduction degree [46]. Synthesis of few layered graphene (FLGp), with enhanced electrical, morphological, and textural properties for the application as anode material in Li ion batteries has also been reported through CVD, microwave exfoliation, and thermal techniques [47–49].

By contrast, the TCVD method is beneficial for the fabrication of large-area devices and promising for future semiconductors made from metal-oxides replacing silica [50]. Epitaxial Gp is another method employed to prepared Gp by applying a thermal process on the surface of Silicon carbide (SiC) [51]. Conversely, this process has some limitations of producing Gp, such as the requirement of high temperature as well as the incapability of heat transfer on other substrates.

Gp has been be synthesized by using two different techniques, either top-down or bottom-up methods [52] as represented in Figure 1.

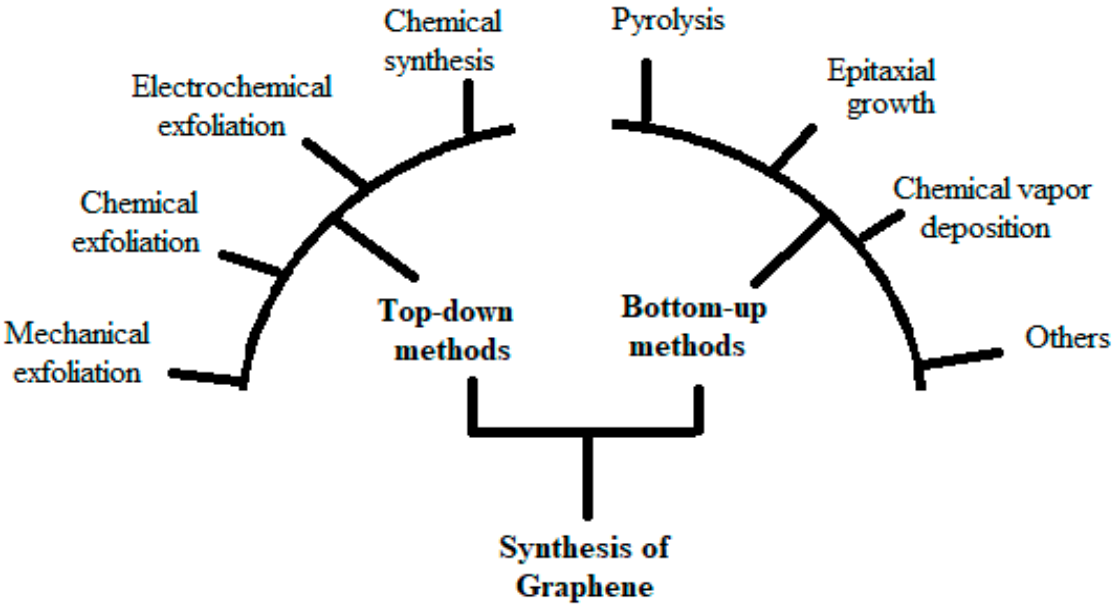

Figure 1. Flow chart for Gp synthetic routes. Reproduced with permission from [52]. Copyright ACS Publications, 2018.

3. Characterization Tools for Gp Materials

Gp has been identified and characterized by different characterization methods such as RS (Raman spectroscopy) that investigates the structure of Gp and TEM (transmission electron microscopy) that helped to distinguish the Gp structure. The SEM (scanning electron microscope) and AFM (atomic force microscope) have been used widely to characterize the morphology of Gp. Methods such as UV-Vis and XRD have been used as advantageous approaches to support the findings.

3.1. Raman Spectroscopy (RS)

RS is considered an important tool for the characterization of Gp [53]. The allotropes of carbon show unique characteristic peaks in RS at approximately 2700, 1580, and 1350 cm^{-1}, respectively [54,55]. These peaks help in determining the number of layers in the Gp. The D and G bands have been assigned to the disorder of carbon of sp^2 nature and tangential stretching mode (E2g) of highly oriented pyrolytic Gr (HOPGr) [56,57]. The 2D band refers to the second-order Raman scattering process [58]. There have been a variety of studies for the synthesis of Gp by chemical reduction process (CRP) that includes an up surged thickness of defects as compared to the other techniques [59]. Figure 2a illustrates the RS of Gr and Gp, and the three characteristics peaks of Gp (2D, G, and D) appeared

at 2680, 1580, and 1350 cm^{-1}, respectively [60]. Generally, Gr and Gp are distinguished by varying intensities of their three characteristic bands as shown in Figure 2a. Besides, the quality of Gp has been reviewed by Raman analysis by estimating the intensity ratio of 2D and G bands. A large I2D/IG ratio and a relatively small D peak amplitude proves that a high-quality Gp was formed [61]. In Figure 2b, Gr prepared by CVD showed a higher intensity ratio than synthesized by ME. Consequently, CVD is considered as one of the most suitable techniques to produce Gp of high-quality [60].

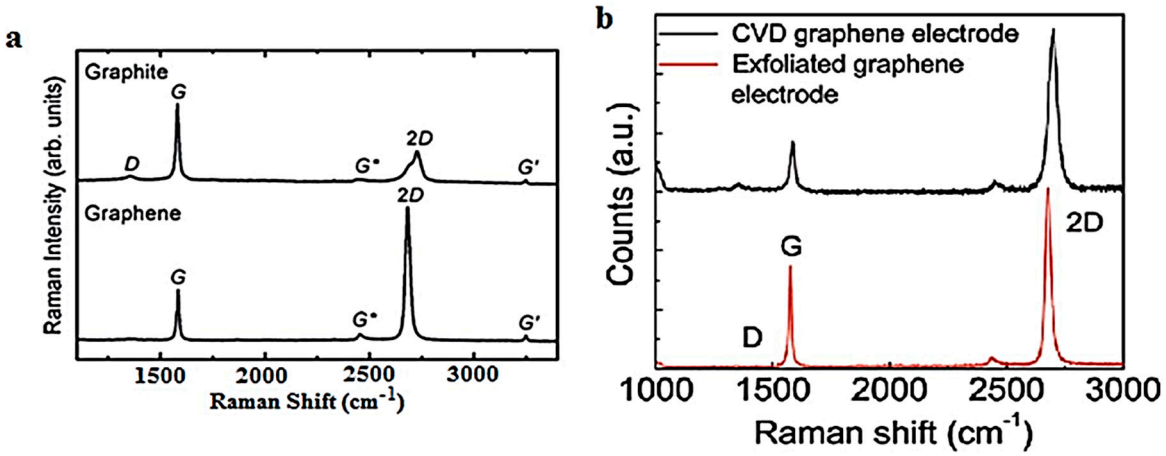

Figure 2. (**a**,**b**) Raman spectra of Gr and Gp. Reprinted with permission from [60]. Copyright RSC Publishers, 2017.

The Raman spectra of FLGp obtained by microwave assisted exfoliation indicated D, G, M-K scattering, 2D, and 2D' bands at around 1352, 1578.6, 2445, 2702, and 3234.3 cm^{-1}, respectively. Furthermore, the intensity ratio I_D/I_G of around 0.6 was assigned to graphitization degree. Whereas, the value of I_G/I_{2D} of 1.2 indicated the presence of less than 20 Gp layers [47]. Likewise, Raman spectra of N-doped Gp foam obtained by CVD process was found to show discrete G and 2D bands at around 1580 and 2705 cm^{-1}, respectively.

3.2. Transmission Electron Microscopy (TEM)

TEM uses electrons in high voltage for transition through a very thin layer of sample and then the reflected signal is received and processed to be in micrograph for observation of morphological variations of Gp [62]. The characterization of Gp using TEM analysis is very imperative due to its capability to capture the image in the nano or even at the atomic level [63]. By analyzing through TEM, single layer Gp is usually considered as a transparent layer. The high and low magnification images of single layer Gp, with the related selected area electron diffraction (SAED) pattern (inset) that displays the hexagonal shape of the crystalline Gp, are shown in Figure 3a,b [60].

Furthermore, FLGp were observed in the TEM images as shown in Figure 4a–f [60]. The SAED patterns (Figure 4g–i) are uneven and not sufficient to justify the multilayers (2, 3, 4, 5, 6, and 7) of Gp. Hence, other characterizations are essential to support the TEM findings.

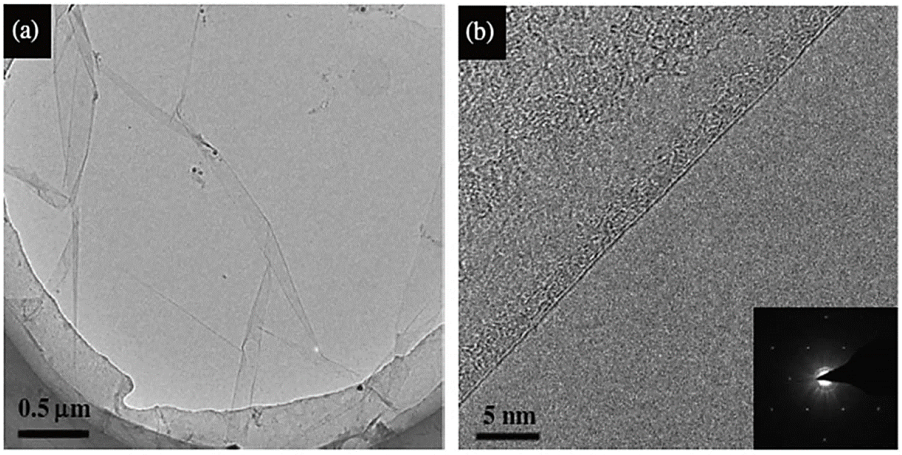

Figure 3. TEM micrographs of single layer Gp at (**a**) low and (**b**) high magnification. Reprinted with permission from [60]. Copyright RSC Publishers, 2017.

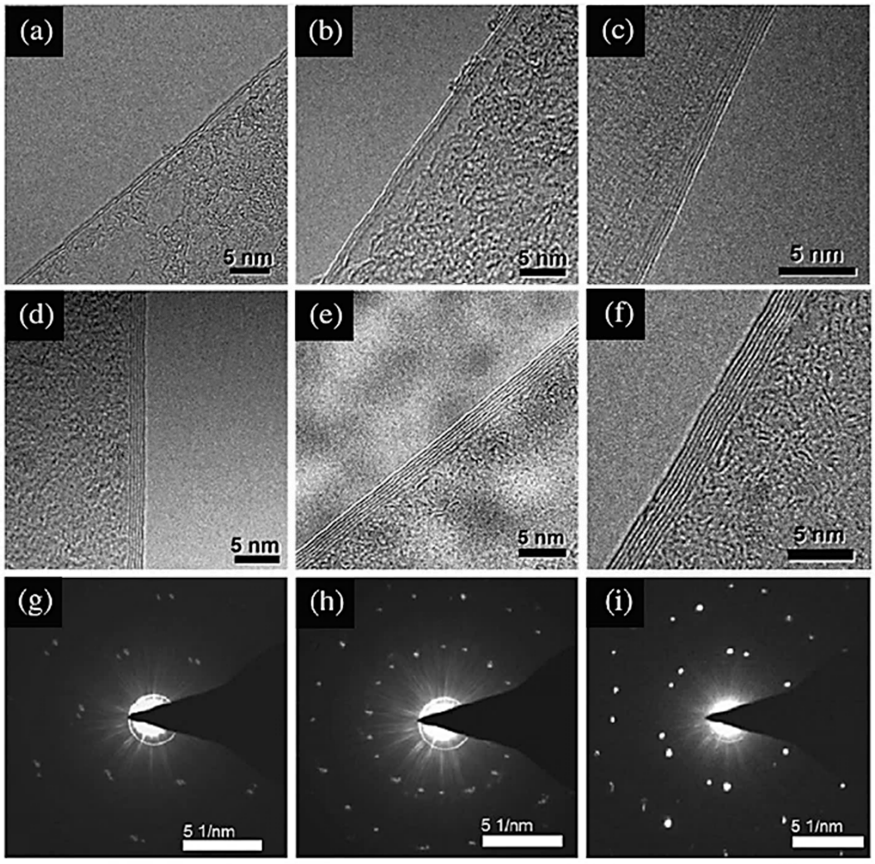

Figure 4. TEM micrographs of Gp edges with different layer numbers: (**a**) two layers, (**b**) three layers, (**c**) four layers, (**d**) five layers, (**e**) six layers, and (**f**) seven layers. The SAED patterns of two, three, and five layers of Gp taken from the center of the domain are presented from (**g**–**i**). Reprinted with permission from [60]. Copyright RSC Publishers, 2017.

3.3. Scanning Electron Microscopy (SEM)

The SEM analysis is extensively utilized to study the morphological characteristics of Gp. The electron microscope and the optical microscope have generally the same principles of working. However, the electron microscope uses the exceedingly exciting electrons as a source instead of the visible light uses in the optical microscope [64]. Besides, the optical microscope has a limited magnification and resolution because of the visible light extensive wavelength source, while the

wavelength of the accelerated electron is much lower than visible light which gives FESEM or SEM a high resolution [65].

Cao et al. have successfully synthesized Gp from natural Gr flakes using Hummers method through liquid oxidization. Following that, a 2-dimensional Gp sheet was observed using SEM. Correspondingly, fold structure was seen on both the edge and the surface of the sample (Figure 5), considered as typical morphology of multilayered Gp [66]. The estimated thickness of the sample was around 100 nm.

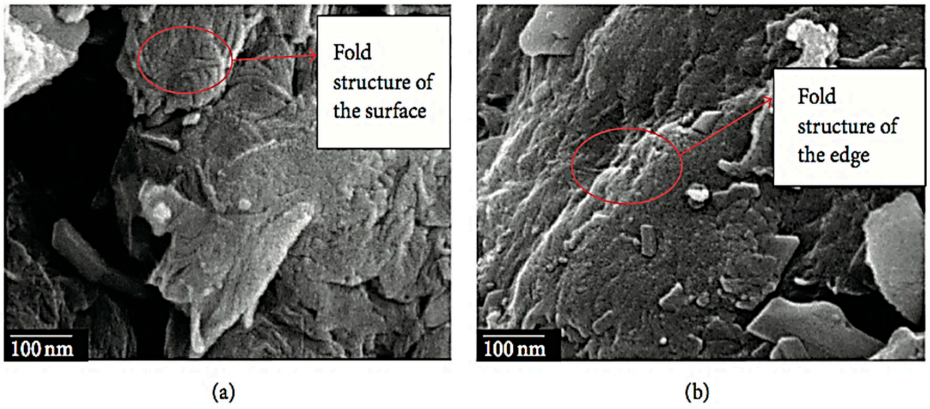

Figure 5. (**a**,**b**) SEM micrograph of synthesized Gp. Reprinted with permission from [66]. Copyright MDPI Publishers, 2015.

Khai et al. [67] synthesized mono to multilayer Gp using a microwave-assisted solvothermal method. The prepared Gp was analyzed using FESEM with an observed dimensional range of 3–10 mm. Figure 6a–d shows single-layer Gp films at low and high magnifications. Besides, surface crumples in the detected sheet and folding at the edges of the Gp films were observed. In contrast, the multilayer Gp was synthesized by Gui et al. [68] using a solvothermal technique. This method has displayed agglomerations and wrinkles which was due to the presence of oxygen-containing functional groups. These results have represented good agreement as reported by Khai et al. that supports earlier studies [67,69].

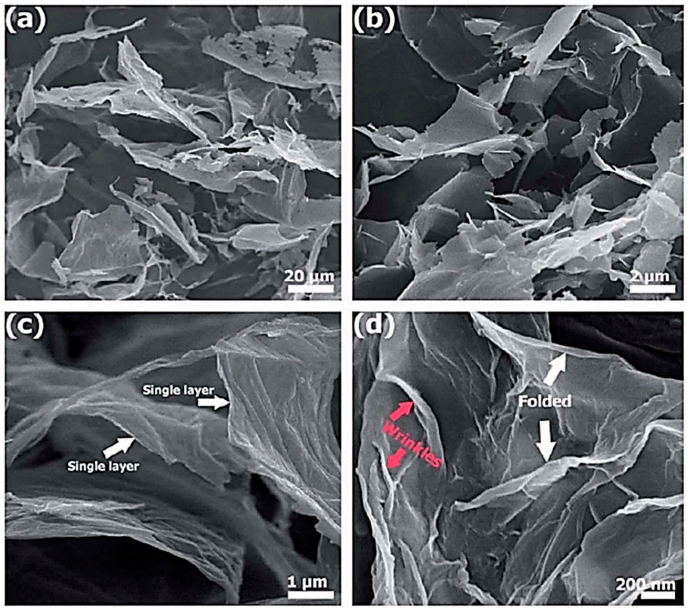

Figure 6. FESEM micrographs of multilayer Gp at (**a**) low, (**b**,**c**) moderate, and (**d**) high magnification. Reprinted with permission from [67]. Copyright Elsevier, 2013.

By employing the CVD method, Hawaldar et al. [70] synthesized a Gp sheet and then analyzed it by using FESEM (Figure 7a). It has demonstrated the wrinkled morphology of the Gp surface (Figure 7b) through FESEM micrograph in high magnification for the Gp double-layer on a copper grid. In another study, the surface area of Gp with growth times of 10 and 15 min has been found higher as observed by Dang et al. [71] (Figure 7c,d).

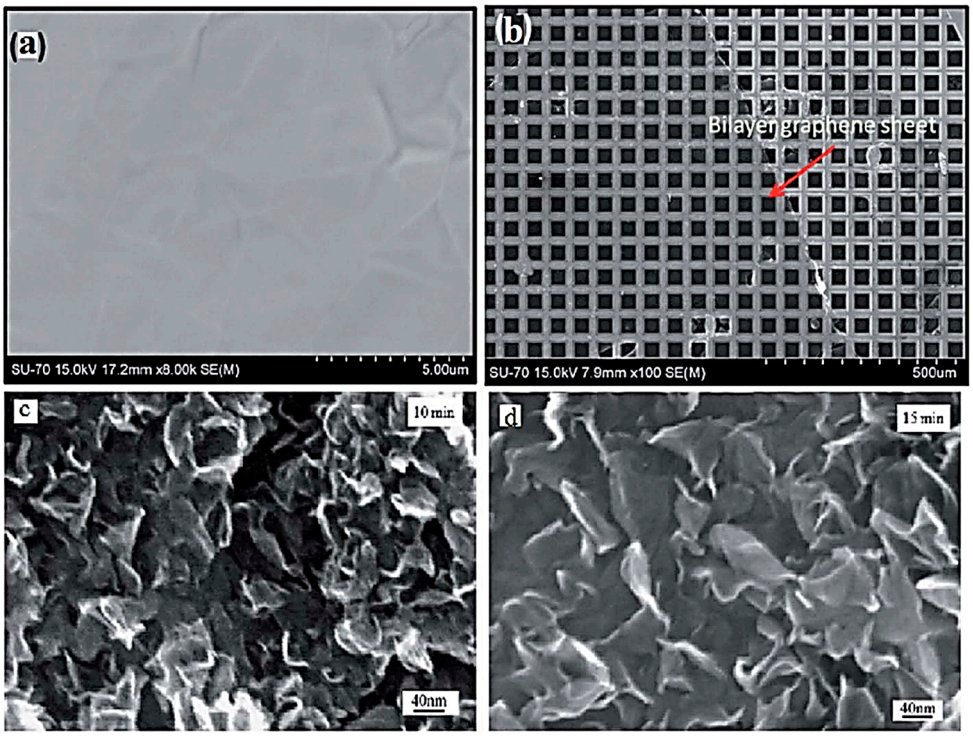

Figure 7. (**a**) FESEM micrographs of Gp sheets grown on copper, (**b**) FESEM micrograph of a double layer Gp sheet on a copper grid, produced by hot filament thermal chemical vapor deposition (high magnification). FESEM micrographs of Gp at (**c**) 10 min and (**d**) 15 min growth times Reprinted with permission from [60]. Copyright RSC Publishers, 2017.

Furthermore, the characterization of Gp using SEM is very popular due to its lower cost as compared to FESEM and its capability to examine the micrographs at moderate magnification. Similarly, Tu et al. [72] examined the surface of Gp film prepared by the CVD method which showed few white wrinkled marks on the surface of the Gp sheet as shown in Figure 8. Petnikota et al. reported that the SEM micrographs of FLGp obtained by microwave exfoliation of Gr has shown the FLGp sheets with lateral dimension of 1 μm^2 and specific surface area of about $\approx$8.2 $m^2 \cdot g^{-1}$ [47]. The morphology of MgO decorated FLGp examined by FESEM was indicated to have MgO spotted on Gp sheets. Whereas, the Gp sheets were exhibited as transparent and semitransparent cubes of varying size [48]. The MgO-FLGp composite exhibited the surface area of 393 m^2/g and an average pore volume of 0.9 cm^3/g.

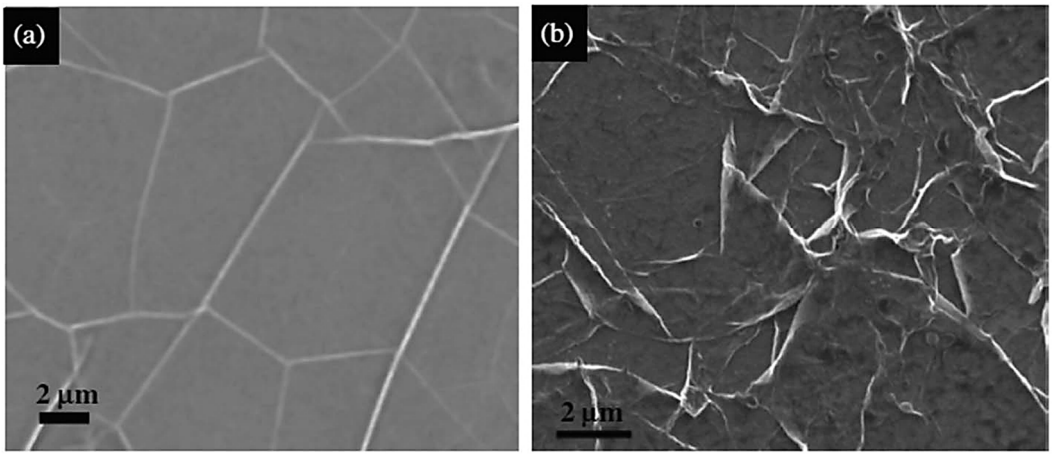

Figure 8. SEM micrograph of a Gp with seven layers on (**a**) Cu substrate and (**b**) Si substrate. Reprinted with permission from [60]. Copyright RSC Publishers, 2017.

3.4. Atomic Force Microscopy (AFM)

Generally, AFM has been employed for the Gp characterization through magnitudes in the nanometer range under diverse conditions, i.e., liquids, ultrahigh vacuum, or normal atmosphere [73]. The roughness and thickness of the Gp have been determined by Lui et al. [74]. Figure 9 displays the Gp synthesized by CVD on four different surfaces using AFM. It has been found that the long reaction time increases the thickness and the surface roughness of the Gp.

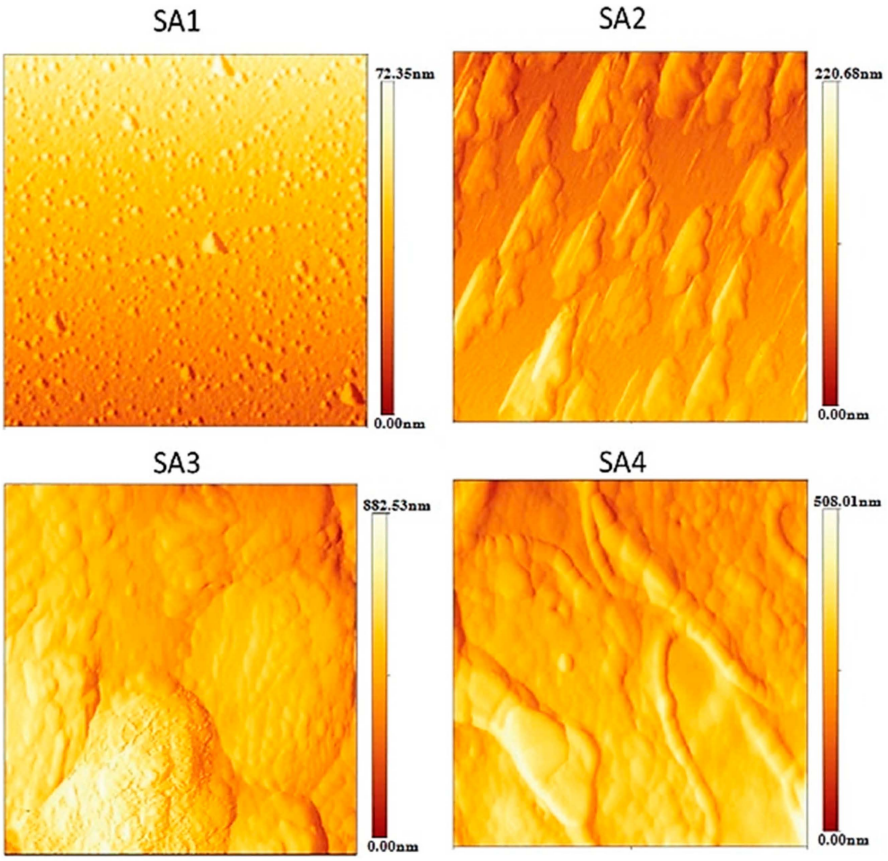

Figure 9. The AFM micrographs of **SA1, SA2, SA3**, and **SA4** were gained in the close contact mode (3 × 3 mm). Reprinted with permission from [60]. Copyright RSC Publishers, 2017.

Gao et al. [75] synthesized the Gp sheet on the substrate of palladium by utilizing the surface segregation process. It was observed by AFM that the uniform shape of the Gp sheet completely covered the palladium surface as shown in Figure 10a,b. However, few carbon nanowires (CNWs) were observed on top of the Gp due to the growth of 3D carbon. The sample edge showed the Gp discontinuity, where the area of an uncovered palladium surface was observed Gp as shown clearly in Figure 10c,d.

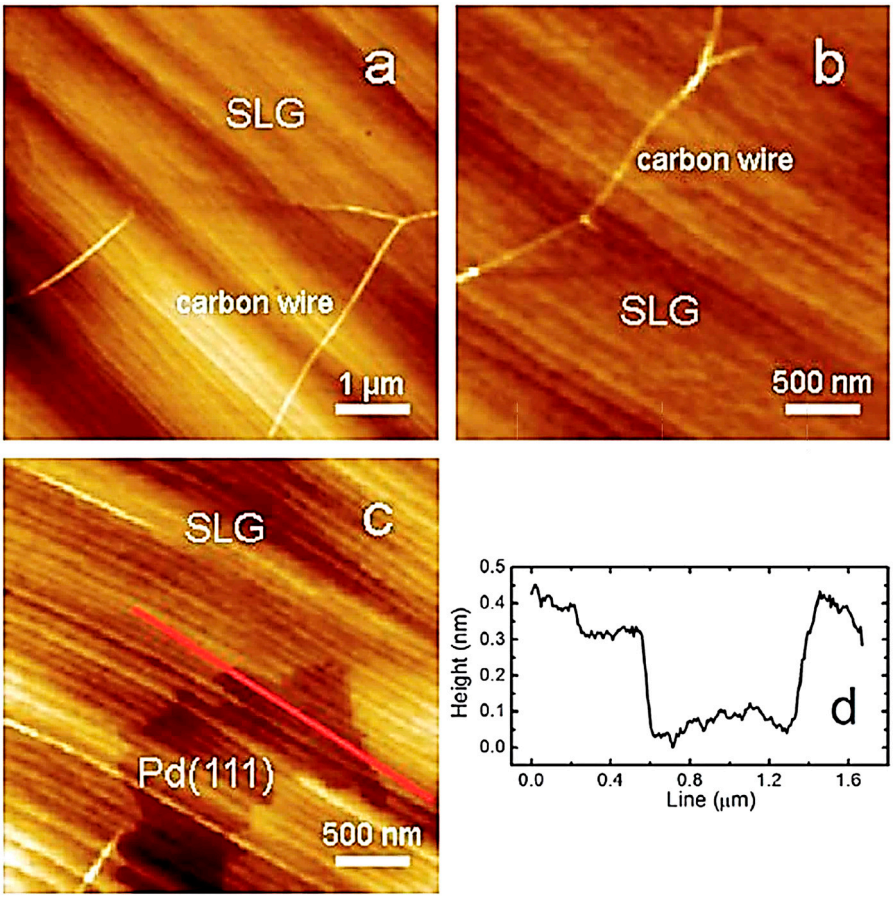

Figure 10. AFM micrographs of Gp produced on Pd (111) substrate. Micrographs (**a**,**b**) were obtained from the center of the Gp sample, micrograph (**c**) was obtained from the edge of the Gp sample, where (**d**) micrograph illustrates the Gp layer height corresponding to monolayer Gp. Reprinted with permission from [60]. Copyright RSC Publishers, 2017.

AFM is considered as one of the effectual methods used to justify the Gp layer thickness. Liu et al. [76] have synthesized multilayer Gp by the exfoliation process on the expandable Gr in a supercritical solvent (N, N-dimethylformamide). Figure 11a,b illustrates the layers of Gp using AFM tapping mode. It can be seen that the thicknesses and sizes are varied while the majority of the Gp sheets areas were approximately 3 nm. Similarly, Figure 11c,d reveals the micrographs of the exfoliated Gp sample with an approximate height of 1.2 nm which suggested the existence of monolayer Gp.

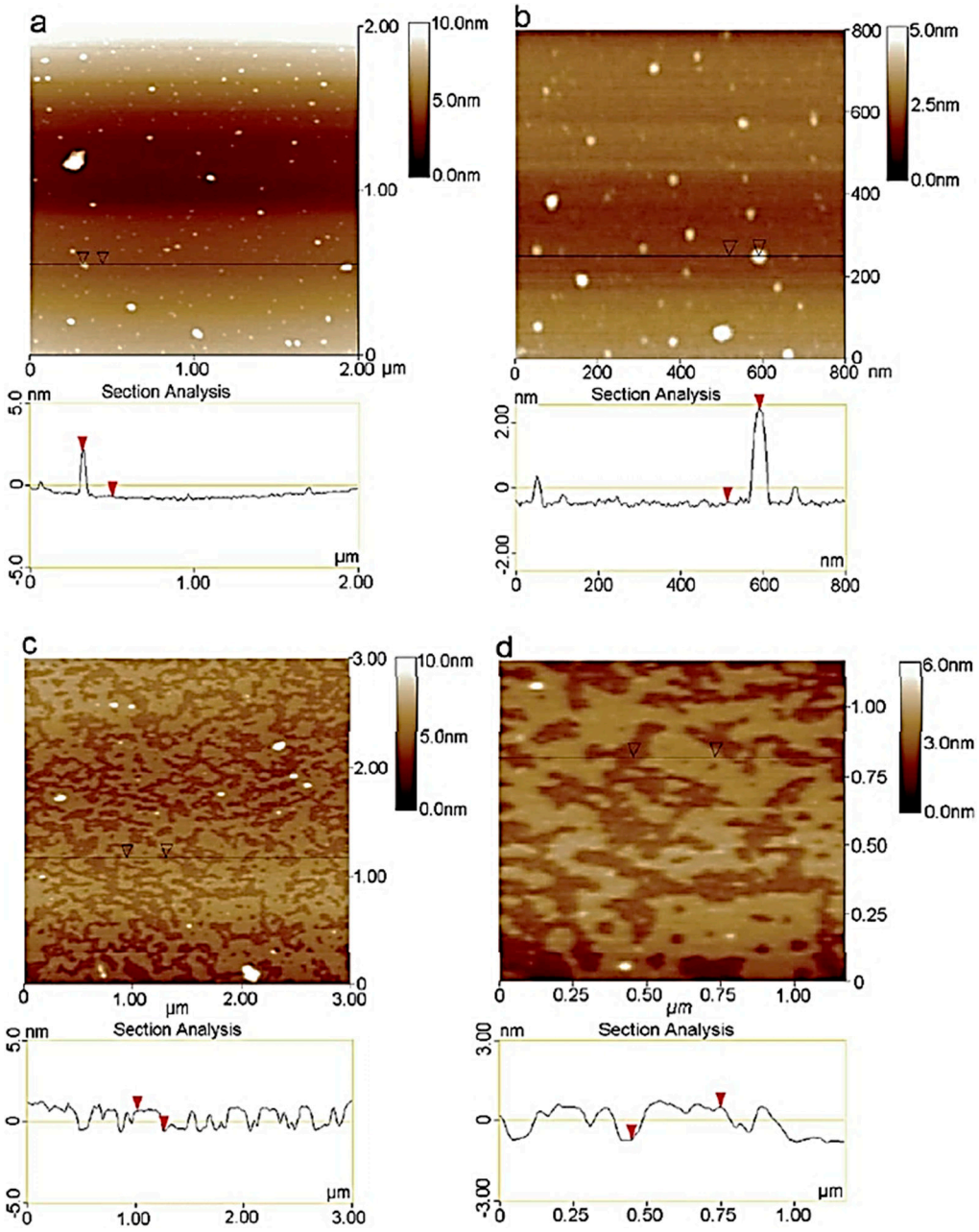

Figure 11. AFM micrographs of (**a**) multilayer Gp films (2 × 2 mm), (**b**) multilayer Gp films (0.8 × 0.8 mm), (**c**) single layer Gp films (3 × 3 mm), and (**d**) single layer Gp films (1.25 × 1.25 mm). Reprinted with permission from [60]. Copyright RSC Publishers, 2017.

3.5. X-ray Diffraction (XRD)

XRD analysis is employed to examine the size, crystallinity, atomic arrangement, defects, and other structural features of materials. X-rays produced by the XRD device are diffracted, scattered, refracted, absorbed, and transmitted through a diffraction pattern [77]. Moreover, Bragg's law helps to determine the atomic planes separation in a material [78]. Each component in the mixture shows different diffraction patterns than other components.

Although XRD analysis is useful for Gp characterization, it is not a sufficient tool to detect the single layer of Gp. Naebe et al. [79] prepared and characterized functionalized Gp, which has better mechanical properties and higher thermal stability than GO. The results of XRD have exhibited Gp, GO, Gr, and functionalized Gp (Figure 12a). A sharp peak of diffraction at $2\theta = 26.5°$ refers to the

pristine Gr with (002) plane of well-ordered carbon atoms and interlayer spacing (d = 3.35 A°) that has disappeared and a new peak at 2θ = 10.5° was observed for GO with d-spacing of 8.41 A°. It has been indicated that large quantities of oxygen atoms are attached on the surface of the GO.

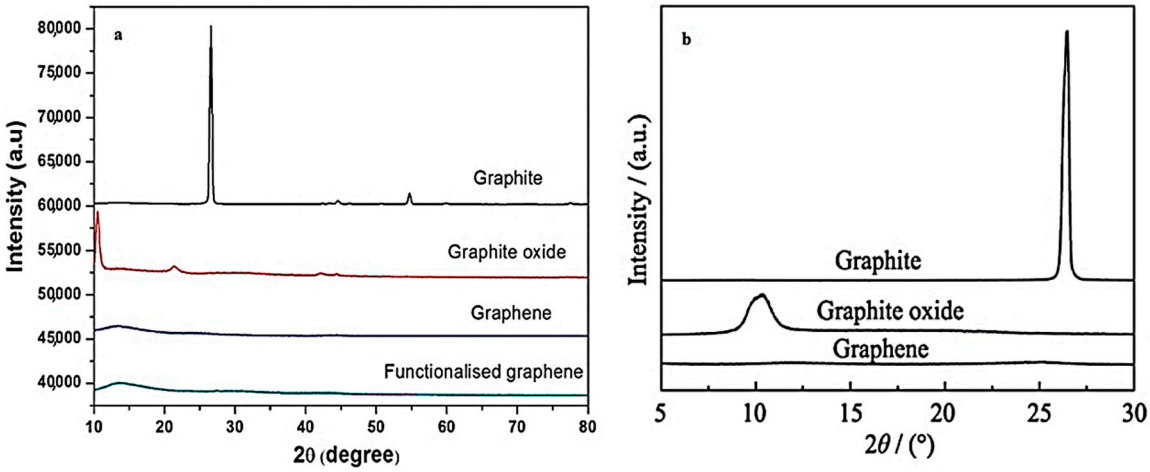

Figure 12. (**a**) XRD pattern for Functionalized Gp, Gp, GO, and Gr, (**b**) XRD plots of Gp, GO, and natural Gr. Reprinted with permission from [60]. Copyright RSC Publishers, 2017.

Consequently, the interlayer spacing of GO is expanded. The functional groups elimination, such as oxygen in GO at a high temperature caused the (002) peak disappearance and the formation of reduced Gp films. Wang et al. [75] have stated that the reduced FLGp film had no (002) peak after microwave irradiation as shown in Figure 12b.

4. Significance of N-Doped Gp for Energy Storage Systems

N-doping improves the physiochemical properties of Gp host materials to enable batteries with superior electrochemical performances. Due to the lone pair of an electron in the outer shell, the N-atom is more electronegative which promotes the electrochemical conductivity and acts as an electrocatalyst for different metal ion batteries [80]. The Li-S technology faces multiple technical issues in terms of the electronically insulating sulfur and the shuttle of its discharge polysulfides products (i.e., lithium polysulfides $Li_2S_{x\ (1,2,3,4)}$). It necessitates polar N-doped host materials to mitigate the shuttle and promote the electrical performance of Li-S batteries [81]. The N-content also leads to enhanced interaction between N-doped materials and Li ions to achieve better performance [82]. In this review, the authors have summarized various synthesis techniques of N-doped Gp materials and emphasized their applications as Li-S, Li-ion, and Metal-Air batteries.

4.1. N-Doped Gp in Conventional Li-Ion Batteries

Lithium metal is considered as the holy grail of all anode materials due to its lowest reduction potential (−3.04 V vs. SHE) and a very high theoretical capacity of ≈3400 mAh g^{-1} [83]. However, the use of Li metal is unsafe due to its (electro-)chemical instability with organic electrolyte. Gr has been a suitable alternative and the first-choice anode material for Li-ion battery (LIB) since the first commercial application by Sony in 1991. Despite the better stability of Gr anodes with conventional electrolytes, a major shortcoming is their limited theoretical capacity (≈372 mAh g^{-1}) that curtails their suitability for high energy applications. Over the years, various other types of carbonaceous materials have been used as anode materials such as Gp, CNTs, carbon nanofibers (CNFs), and so on. Nevertheless, the intrinsic limitation of lower storage capacity remains. In this regard, chemical doping of such materials with various dopants such as P, B, and N is an effective strategy.

Approaches of various defects have been created in the materials rendering them higher Li^+ ion storage sites and boosting the specific capacity of the electrodes. In particular, N-doping is

advantageous since N-atoms are more electronegative than carbon atoms which ensures stronger interactions with Li-ions. Reddy et al. [84] demonstrated the growth of N-doped Gp layers through liquid precursor-based CVD method using hexane and acetonitrile. The electrodes were prepared by directly growing the N-doped Gp on copper current collectors. Results demonstrated a two-fold increase in the specific capacities for the N-doped Gp electrodes when compared with pristine Gp. The enhanced capacity was attributed to the improved Li-ion mobility due to a higher number of surface defects caused by N-doping. By simple pyrolysis of polypyrrole and GO nanosheet as a precursor, a micro/mesoporous structure of N-carbon/rGO was derived with a specific surface area of 327 m^2 g^{-1} (Table 1). While tested as anode, the electrodes delivered a good reversible capacity of ≈750 mAh g^{-1} at 100 mA g^{-1} for 200 cycles (Figure 13a,b) which was significantly higher than that of N-carbon (Figure 13c). Comparing the Nyquist plots of both electrodes, N-carbon/rGO demonstrates much lower resistance as shown in Figure 13c.

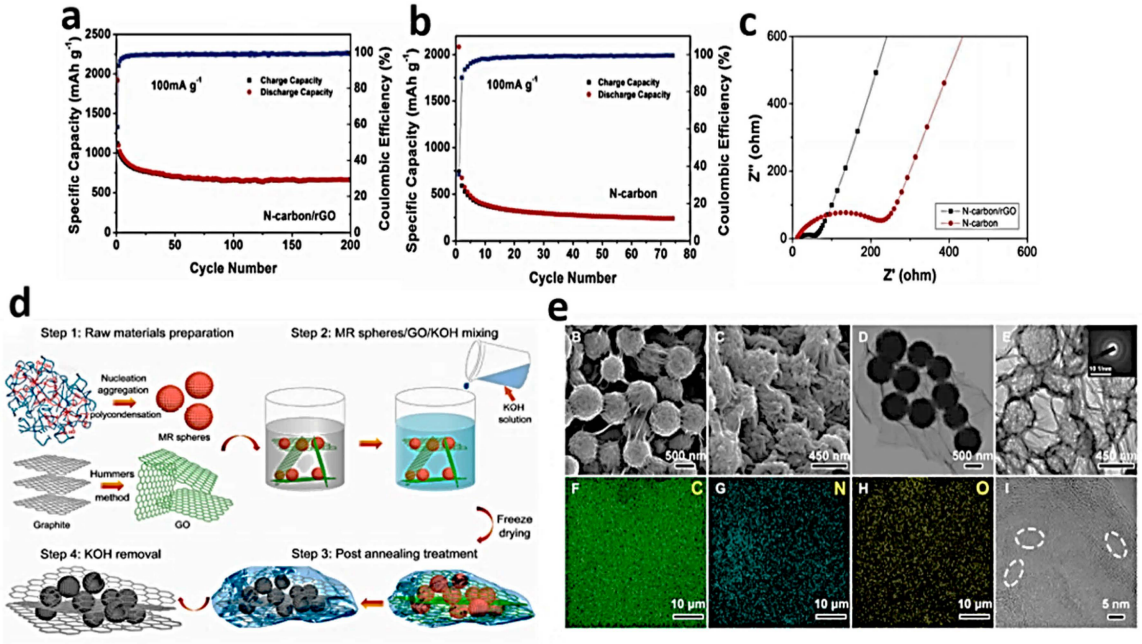

Figure 13. Battery cyclic performance (**a**) N-carbon/rGO; (**b**) N-carbon; (**c**) Nyquist plots for N-carbon/rGO and N-carbon [85], (**d**) schematic depiction of the synthesis procedure of DHCSs/RGO composites, (**e**) SEM images of (B) MR spheres/GO after mixing (C) DHCSs/RGO-700; TEM images (D) MR spheres/GO and (E) DHCSs/RGO-700. (F−H) Elemental mapping of DHCSs/RGO-700 (I) HRTEM image of DHCSs/RGO-700 Reprinted with permission from [52], Copyright ACS Publisher, 2018.

Efforts are also underway to design 3D structures based on carbon materials such as GO. Hollow carbon spheres/rGO are developed by compositing with poly(vinyl alcohol) (PVA) through polycondensation of oligomers (melamine and formaldehyde) followed by the KOH activation/reduction of the nanocomposite (schematic Figure 13d) [52]. The morphology and composition of the 3D structures was confirmed by SEM/TEM images and elemental mapping (Figure 13e). The usage of DHCSs/RGO exhibited an excellent capacity of 1395 mA h/g at 0.1 A/g and 606 mA h/g at 5 A/g as anode materials. Multiwalled N-doped CNTs have also been synthesized and characterized for LIB applications. Bulusheva et al. [86] reported the synthesis of CNTs through the aerosol-assistant catalytic CVD method. The authors used toluene and acetonitrile for nanotube morphologies and N-contents. They found the highest reversible capacity of 270 mAh g^{-1} at the current density of 0.2 mA cm^{-2} and the highest value of exchange current density at the lowest N-content of (≈1 at. %). Reportedly, Tin (IV) oxide nanocrystals (SnO_2-NCs) have been embedded with N-doped rGO sheets through in situ hydrazine monohydrate vapor reduction method [87].

When tested for LIB, the SnO_2NCs@N-rGO exhibited excellent discharge capacity, cycle life, and rate capability. In another work, N-doped Gp-CNTs lamellar architecture was utilized as anode material for LIB [88]. The N-content was 11.1% that resulted in a high surface area of 293 m^2g^{-1} (Table 1). The unique architecture and N-doping helped in achieving a high reversible capacity of ≈500 m Ahg^{-1} at a current density of 1 Ag^{-1}. Sui et al. [82] synthesized Gp-based hydrogel using N-doped porous Gp. The Gp/melamine-formaldehyde hydrogel was freeze-dried followed by thermal treatment. The material exhibited a higher discharge capacity (672 mAh g^{-1}) as compared to N-free Gp porous material (450 mA h g^{-1}) at a current density of 100 mA g^{-1}. Further, the initial capacity was retained for 200 charge/discharge cycles at 400 mA g^{-1}. Through pyrolysis of polypyrrole/GO nanosheet precursor, N-doped carbon/rGO was synthesized and used as anode material for LIBs [85]. The N-content was doped up to 15.4%, which helped in obtaining micro/mesoporous structures with a high specific surface area of 327 m^2 g^{-1}. The materials exhibited a reversible capacity of 1100 mA h g^{-1} at 100 mA g^{-1} and cyclic stability (1000 cycles) at a high current density of 1 A g^{-1}. Another unique synthetic route of Gp preparation was evaluated by Puttapati et al. using sunlight converged through lenses on GO [89]. Solar rGO was introduced as an excellent anodic material for Li-air batteries. The exhibited discharge and charge capacities were 1480 and 880 mAh g^{-1}, respectively. Moreover, an elevated current density of 100 mA g^{-1} was tested with columbic efficiency >95% and specific capacity of ≈500 mAh g^{-1} even after 60 cycles. It was displayed as reliable and excellent Li storage material.

Goh et al. [49] synthesized the N-doped Gp foam by using eggshells in the Gp foam (GE/GF) through CVD process. The GE/GF anode exhibited the first discharge capacity of 424 mAh g^{-1}, and the reversible capacity was 328 mAh g^{-1}, while the capacity enhanced to 368 mAh g^{-1} at 45 cycles. The cycling stability of electrode revealed the initial Coulombic efficiency which increased to 77.5%. It suggested the in-filling of foam by Gp eggshell which decreased the decomposition of electrolyte and the surface side reactions.

4.2. Role of Gp-Based Materials in LSBs

Reportedly, Gp-based materials have been used to enhance the performance of LSBs [90,91]. The insightful role of these materials has been indicated by using 2D g-C_3N_4/Gp composite, which showed the discharge capacity of 612.4 mAh g^{-1} at 1 C after 1000 cycles [92]. Similarly, Gp nanoflakes implanted sulfur cathode CoP@G/CC-S have been reported to offer a discharge capacity of 930.1 mAh g^{-1} at 3 C and a real capacity of 8.81 mAh cm^{-2} at 0.05 C with increased sulfur loading (up to 10.83 mg cm^{-2}) [93]. 3D-rGO with host Li_2S_6 catholyte has been also used with discharge capacity 1607 mAh g^{-1} at 0.1 C and efficiency of over 200 cycles with sulfur loading 6.6 mg cm^{-2} [94]. Designed sulfur cathodes using Gp with the effect of particle sizes of 13 µm and 500–1000 nm [95], Gp embedded WS_2 nanoclusters (degradation 0.067% per cycle at 1 C during 250 cycles) with sulfur loading (10.83 mg cm^{-2}) [96], and Gp sheets grafted with $Ni_{12}P_5$ nanoparticles (degradation 0.074%/cycle at 1 C during 500 cycles) with sulfur loading (3.5 mg cm^{-2}) [97], have also been reported.

Likewise, other Gp based materials such as Gp quantum dots with 99% efficiency (capacity 3mA cm^{-2} and sulfur loading (4 mg cm^{-2}) above 200 cycles [98] and Gp compounded with $LiFePO_4$ sulfur cathode for enhanced sulfur loadings (4.3–8.4 mg cm^{-2}) [99] have presented a great potential to advance electrochemical performance and amplified charge transfer with elevated properties of energy storage among LSBs.

4.2.1. Li-Sulfur Batteries

Li-sulfur (Li-S) chemistry offers much higher energy densities than the current Gr and $LiCoO_2$ based LIBs. Efforts are underway to improve the Li-S system by addressing various issues associated with the S cathode including lower electronic conductivity of S, loss of active materials due to polysulfide shuttle, and high volumetric expansion of S during Li insertion/de-insertion [100]. The use of Gp-S composite has been shown as an effective strategy to solve the aforementioned issues [101]. The doping of Gp in particular with N atoms increases the conductivity and enhances surface interaction with

polysulfides at molecular interactions. The process immobilizes such polysulfides species which can greatly improve the electrochemical performance of the batteries [102].

Recently, N-doped Gp and CNTs as sulfur host advances the cycling performance with discharge and retention capacity of 1465.1, 1315.1, and 849.1 mAh g^{-1} after 200 and 500 cycles, respectively, at 1.0 and 2.0 C [103]. Additionally, N-doped Gp porous cables have been utilized the sulfur cathode and lithium anode as another example with a capacity of 525 mAh g^{-1} and degradation of 0.14% per cycle over 100 cycles at 0.5 C [25]. Additionally, N-doped graphitic electrodes also have been found promising such as cathode (capacity 1473 mAh g^{-1}, degradation 0.075% above 500 cycles at 0.5 C) with sulfur loading (3 mg cm^{-2}) and the cathode (capacity 833 mAh g^{-1} above 120 cycles at 1 C) with sulfur loading (6 mg cm^{-2}) [104]. Likewise, optimization of N-doped Gp (discharge capacity 1311 mAh g^{-1} at 0.2 C, capacity: 950, 762, and 580 mAh g^{-1} at 1, 2, 3 C) with sulfur loading (4 mg cm^{-2}) has been observed [105]. Moreover, cobalt in N-doped Gp for high sulfur content (capacity 1210 mAh g^{-1}, degradation 0.029% over 100 cycles at 0.2 C) with sulfur loading (6 mg cm^{-2}) [106] and N, sulfur co-doped Gp augmenting $Li_4Ti_5O_{12}$ anode (capacity 130 mAh g^{-1} at 80 C and 123 mAh g^{-1} at 100 C) displayed cathode (89.5% retention capacity above 500 cycles at 5 C) [94], have shown multifunctionality to accelerate redox kinetics among LSBs electrodes. Wang et al. demonstrated outstanding performance of 3D N-doped Gp and S composite (3D-NGS) cathodes [107]. A high amount (87.6 wt%) of S was loaded in N-Gp via a facile one-pot solution method as shown in Figure 14a. The amount of N was 10% and the surface area of the Gp was 398 m^2 g^{-1} (Table 1). The cathodes exhibited a capacity of 671 mA h g^{-1} after 200 cycles at a high current of 1500 mA g^{-1} (Figure 14b).

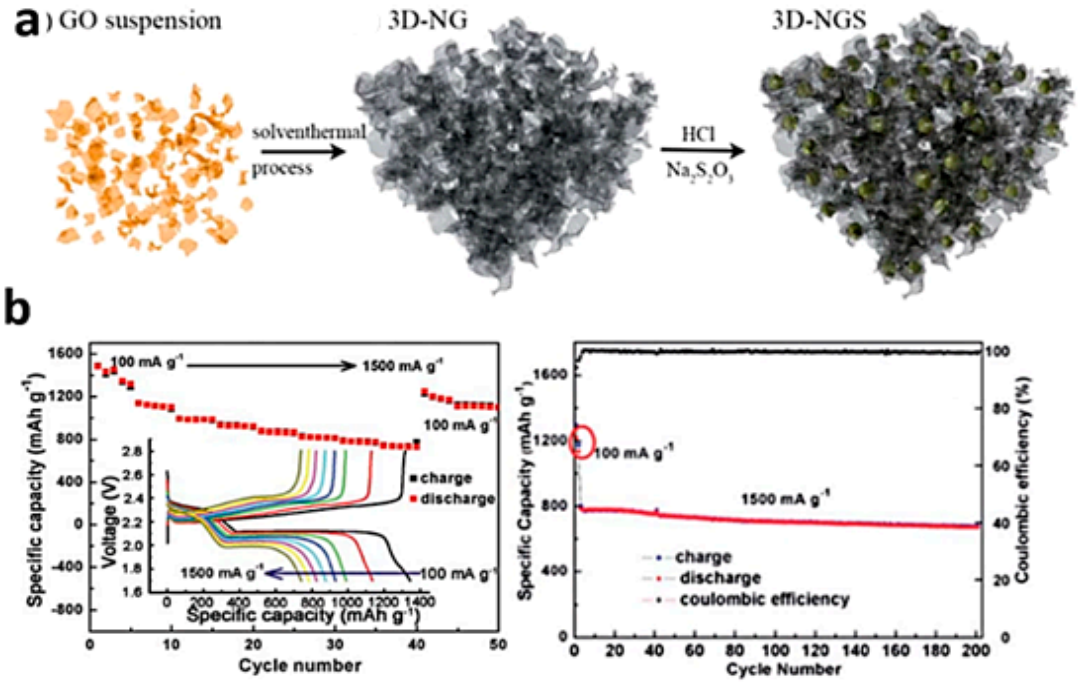

Figure 14. *Cont.*

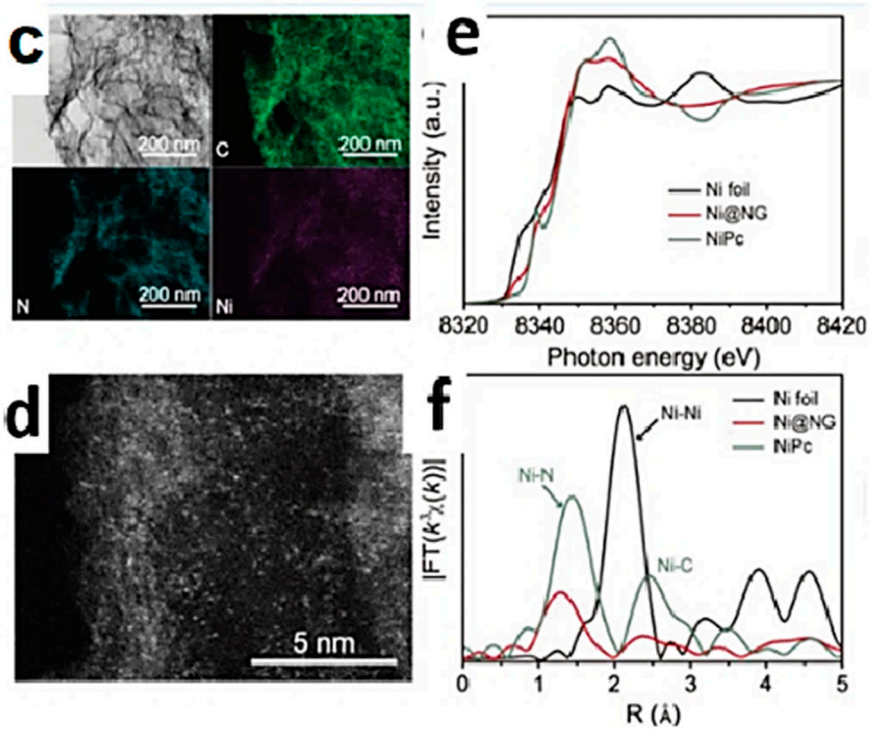

Figure 14. (**a**) Schematic of the synthesis of 3-dimensional N-doped Gp-S composites and (**b**) rate and cyclic performance (**c**) TEM and the corresponding element mapping images of Ni@NG; (**d**) the sub-angstrom resolution HAADF-STEM image of Ni@NG, (bright spots represent single Ni atoms); (**e**) XANES; (**f**) FT-EXAFS spectra Reprinted with permission from [107]. Copyright RSC Publishers, 2014.

Tang et al. [108] proposed a 3D sandwich-like hierarchical design based on aligned CNTs and Gp layers (N-ACNT/G). They claimed that the architecture provides 3D electron transfer pathways and ion diffusion channels. Further, N-doping (0.8%) with more defects and active sites were introduced in the structures that enhanced the electrochemical interactions with the PS. Li-S battery based on the N-ACNT/G cathode materials delivered a high initial reversible capacity of 1152 mAh g^{-1} at 1.0 C, maintaining ca. 76% initial capacity after 80 cycles. In another work, Zhang et al. [109] embedded single nickle (Ni) atoms on N-doped Gp (Ni/NGp) and utilized them as the separators for Li–S batteries. The idea was to trap polysulfides by the oxidized Ni sites of the Ni–N4 structures. Further, the kinetic conversion of the Li polysulfides during the charge/discharge is accelerated due to low free energy and decomposition energy barrier that was possible by the charge transfer between the polysulfides and the oxidized Ni sites. Figure 14a shows the schematic of the synthesis process where Ni @NG was prepared with Ni-N4 sites through a pyrolysis approach. Porous structure is confirmed in Figure 14c while the high-angle annular dark field-scanning transmission electron microscopy (HAADF-STEM) confirmed the presence of Ni atoms (bright dots (≈2–3 Å) on NG (Figure 14d). The cationic coordination environment of the middle Ni sites is confirmed by the X-ray near-edge absorption fine structure spectra (XANES), where the absorption edge position of Ni/NGp is located between those of the Ni foil (Ni^0) and the NiPc (Ni^{II}) as shown in Figure 14e. Furthermore, through Fourier transform extended X-ray absorption fine structure (FT-EXAFS) spectra (Figure 14f, Ni-N rather than Ni-Ni bonding was confirmed. All these characterizations confirmed the presence of Ni atoms in a well-distributed fashion in the N-doped Gp structures. With such Ni/NGp modified separators, an excellent Li–S battery was achieved where stable cycling life with only 0.06% capacity decay per cycle was observed. A similar approach of Ni atoms on N-doped Gp and CNTs have also been shown in other work where the modified separator achieves good electrochemical Li-S performance [110].

4.2.2. Significance of Lithium-Sulfur Batteries

Over the years, gradual development in cathode/anode and electrolytes have incorporated sulfur as a promising material in LSB. In this regard, the desirable energy properties of sulfur-based materials such as explicit capacity of 1675 mAh g^{-1}, frequency and energy density up to 2600 Wh Kg^{-1} have played a vital role [111,112]. Due to the sulfur low cost and high compatibility towards energy storage applications, the emergence of LiS batteries has improved [113]. In recent times, various impactful studies of carbon-derived materials (CDM) have developed to ensure the progress of sulfur cathode, Li anode, electrolytes, and separators, for a variety of materials [114–116]. Particularly, sulfur treatment, functional binder, functional interlayer, and SEI layer have been observed through the adaptation of functional sulfur host, modified electrolyte, and modified separator [117,118]. Similarly, the electrochemical performance of LSBs has been manipulated through polymer materials such as polymer cathodes (polypyrrole, polyaniline, polythiophene), organosulfur polymers, polymer binders, polymer electrolytes (polyvinylidene difluoride, polyethylene oxide), and polymer interlayers (Nafion, polyacrylic acid, polydopamine) [119].

Due to the momentous polysulfide shuttle effect of sulfur cathode [120], various other nanomaterials such as V_2O_5 nanosheets fabrication with specific capacity (838.8 mAh g^{-1}, 200 cycles, 0.1 C) [121], lithiation by combining $FePS_3$ flakes with excellent cycling stability (current density 1 C, decay of 0.04%/cycle up to 1000 cycles) [122], assembling N-doped carbon shell-CeO_2 nanoparticles (reversible capacity of 1348 mAh g^{-1} at 0.2 C, cycle stability of 632 and 458 mAh g^{-1} at 2 and 5 C after 500 cycles) with high sulfur loading (3.5 mg cm^{-2}) [123], metal-organic frameworks derived molybdenum carbide-CN-octahedrons (decay rate of 0.0457%, 600 cycles at 1 C, cycle capacity of 807 mAh g^{-1}) with high sulfur loading (4.2 mg cm^{-2}) [124], novel S/$MoSe_2$/MoO_2 along with 66% sulfur content (1100 mAh g^{-1}, 77% capacity retention after 500 cycles 0.5 C) [125], to enable high performance of LSBs.

4.2.3. Role of N-Doped Gp in LSBs

Significant attempts have been made to boost the efficiency of LSBs using N-doped Gp. In this regard, N-doped Gp based lithium sulfur batteries (LSBs) have stated bulk energy storage applications [126]. Recently, N-doped Gp and CNTs as sulfur host (discharge capacity 1465.1 mAh g^{-1} at 0.1 C, stability of 1315.1 and 849.1 mAh g^{-1} over 200 and 500 cycles, respectively, at 2.0 C) [103], N-doped Gp porous cables for sulfur cathode and lithium anode (energy density of 10.2 m Wh cm^{-2}, capacity 525 mAh g^{-1}, degradation 0.14% per cycle over 100 cycles at 0.5 C) [127], N-doped graphitic electrodes such as cathode (capacity 1473 mAh g^{-1}, degradation 0.075% above 500 cycles at 0.5 C) with sulfur loading (3 mg cm^{-2}) and cathode (capacity 833 mAh g^{-1} above 120 cycles at 1 C) with sulfur loading (6 mg cm^{-2}) [104], optimization of N-doped Gp (discharge capacity 1311 mAh g^{-1} at 0.2 C, capacity: 950, 762, and 580 mAh g^{-1} at 1, 2, 3 C) with sulfur loading (714 mAh g^{-1} at 1.5 mA cm^{-2} above 400 cycles for 4 mg cm^{-2}) [105], cobalt in N-doped Gp for high sulfur content (capacity 1210 mAh g^{-1}, degradation 0.029% over 100 cycles at 0.2 C) with sulfur loading (6 mg cm^{-2}) [106] and N, sulfur co-doped Gp augmenting $Li_4Ti_5O_{12}$ anode (capacity 130 mAh g^{-1} at 80 C and 123 mAh g^{-1} at 100 C) displayed cathode (89.5% retention capacity above 500 cycles at 5 C) [128], have shown multifunctionality to accelerate redox kinetics among LSBs electrodes.

Table 1. Electrical properties of various carbon-based materials.

N-Doped Electrodes	Current (mA g^{-1})	Reversible Capacity (mA h g^{-1})	Voltage Window (V)	Initial Coulombic eff. (%)	N-Content	Surface Area (m^2 g^{-1})	Ref.
Gp nanosheets	42	900	0.01–3.0	-	2%	-	[129]
CNFs	100	1280	0.01–3.0	48.4	10.25 wt%	2381	[130]
Mesoporous carbon	100	1780	0.01–3.0	55	10.1 wt%	805.7	[131]
Porous carbon	100	1181	0.01–3.0	55	5.5%	1300	[132]
Porous Gp	100	742	0.01–3.0	62%	5.8 at%	1170	[82]
Carbon nanosheets	100	1913	0.01–3.0	49.2%	4.7%	2494	[133]
Gp nanoribbons	100	740	0.01–3.0	63%	3.7 at%	-	[134]
Gp nanosheets	100	832.4	0.01–3.0	44.8%	19.46 at%	504	[135]
CFs	30	650	0.005–3.0	82.8%	12.6 wt%	381	[136]
Carbon sponge	500	553	0.001–3.0	34.7%	2.38 at%	613	[137]
Carbon spheres	500	666	0.01–3.0	60%	5%	67.4	[138]
Carbon capsules	50	1046	0.01–3.0	90%	13.3%	595	[139]
Gp frameworks	200	700	0.005–3.0	52.3%	2.6 wt%	610	[140]
Gp microspheres	100	1643	0.005–3.0	66.9%	9.63%	948	[141]
N-doped Gp	50	1177	0.01–3.0	-	2.1 at%	-	[142]
Carbon/rGO	100	1100	0.003–3.0	58.3%	15.4 wt%	327	[85]
Gp/N-doped carbon nanosheets	500	554	-	-	-	-	[85]
Gp/CNTs nano-lamellar design	1000	≈550	0.01–3.0	60.1%	11.2 at %	293	[88]
3D-Gp	1500	≈670	1.7–2.7	≈100%	10.1 at%	398	[107]
CNTs/Gp sandwich design	1C	≈1150	1.6–3	≈98%	0.86	217	[108]

4.3. N-Doped Gp Materials for Metal-Air Chemistries

While LIBs continue to dominate the energy storage market, serious doubts remain on their suitability to fulfill the needs of high energy applications such as electric vehicles and grid-storage. The expansion of storage systems based on LIBs to reach higher energy density values suitable for transportation is unlikely to happen due to the limited electrode charge/discharge capacities. This demands development of new chemistries that can overcome such limitations. Due to their tremendous capacity in terms of higher energy densities, metal-air batteries have gained considerable interest as alternative storage devices. Gp derivatives have been examined as promising electrodes due to their high electron mobility of up to 15,000 $cm^2/V{\cdot}S$ at atmospheric conditions. Electrodes are composed of highly porous materials which allow ions movement and high capacitance.

Gp derivatives have been examined as promising electrodes due to their high electron mobility of up to 15,000 $cm^2/V{\cdot}S$ at atmospheric conditions. Electrodes are composed of highly porous materials which allow ions movement and high capacitance. For example, compared to the current LIBs, practical Li-air batteries have been offered three times higher energy density (in the range 500–900 $Whkg^{-1}$). Metal-air batteries include Li-air [143], Zn-air [144], and Al-air [145] chemistries. An attractive feature of a metal-air battery is the use of an air electrode with an open structure to draw O_2 from the air that is the cathode active materials. With O_2 from air as the main reactant, a significant reduction has been achieved in the weight and volume of the battery pack making it suitable for EV applications.

The metal air batteries consist of an electrochemical cell, which applies oxidation of metal at the anode and reduction of oxygen at the cathode to produce a current flow. The process has challenged in optimal oxygen evolution reaction (OER) and oxygen reduction reaction (ORR), generally termed as charge and discharge for the metal-air battery system. Air cathode, the catalyst for O_2 reduction reaction, is mainly the limiting factor of metal-air batteries. Carbon-based nanomaterials have been used as suitable catalysts since the porous carbonaceous structures with high surface areas provide more active sites for electro-catalysis. In earlier studies, Gr was a commonly used anode material in Li-air batteries. However, it has shown relatively low specific capacity and high Coulombic efficiency. Due to that, it was necessary to come up with novel Gp derivatives such as N-doped Gp which integrates elevated capacitance and energy density among batteries [146]. Further, improved catalytic properties have been achieved by N-doping since graphitic carbon can induce a +ve charge on the adjacent carbon atoms by increasing oxygen absorption and fracture of O-O bonds. Reportedly, N-doping has

encapsulated with Gp layers as a great electron transfer medium. Thus, improving its mechanical properties, durability, and stability to display promising cycling capacitance as anode materials in Li-air batteries [147]. Zhou et al. [148] demonstrated a 3D N-doped porous Gp foam (PNGFs) as an efficient catalyst for ORR. A hard-templating approach was adopted as depicted in schematic Figure 15a. The electrochemical activity of PNGFs was demonstrated by CV measurements (O_2 and N_2 saturated 1 M KOH). As shown in Figure 15b a double layer capacitive behavior is observed under N_2 saturation, however, with O_2 saturation a clear cathodic peak at ≈1.02 V vs. RHE is observed confirming the high catalytic activity of the samples towards ORR. Further, LSV conducted through rotating disk electrode measurements demonstrated better electrocatalytic activities for PNGFs when compared to other samples (Figure 15c). Yun et al. [149] reported the formation of scalable graphitic carbon quantum dots (CQDs) for the application of novel N-doped CQDs also known as the rGO. These porous Fe_2O_3 (N-CQDs/rGO/Fe_2O_3) demonstrated fascinating electrochemical properties, specific capacity, and extraordinary cycling performance. From various contents of Fe_2O_3, 34.9 wt% Fe_2O_3 was found to have the optimal properties like rate capability (72.1%, 58.9%, and 46.2%) and capacity of retention (5, 50, and 100 A g^{-1}), whereas the cycle performance was 80.4% capacity retention at 3 A g^{-1} over 5000 cycles. Similarly, Ferrous-cluster implanted in nanoparticles of Fe_3C as Fe_3C(Fe) in N-doped graphitic layers (NDGLs) exhibited maximum power density of 186 mW cm^{-2} when used for zinc-air battery, which was higher than the Pt/C catalyst (167 mW cm^{-2}) for the same system [150]. N-doped Gp foam has also been utilized for Zn-air batteries [151]. The schematic depiction of the synthesis procedure is shown in Figure 15d. The prepared N-doped Gp foam-carbon fiber paper (NGF-CFP) exhibited favorable oxygen electrocatalysis. In the same study, NGF-CFP was reported to provide a current density of 10 mA cm^{-2} at 2.16 V (charging) and 1.12 V (discharging), respectively. N-doped graphitic carbon (Mn$x$$Fe_{3-x}$C/NC) was encapsulated with manganese−iron binary carbide (Mn$x$$Fe_{3-x}$C) NPs through facile pyrolysis of zeolitic imidazolate framework (Fe, Mn, Zn) [152]. The results showed an energy density of up to 762 mWh g^{-1}, power density of 160 mW cm^{-2} at 250 mA cm^{-2}, open-circuit voltage of 1.5 V, and stability over 1000 cycles when tested for Zn-air battery.

Yang et al. [153] reported the synthesis of metal-free N-doped Gp-based 3D nanoribbon networks (N-GRW) for ORR-OER metal-air battery systems. The zinc-air batteries showed an open-circuit voltage of 1.46 V, a specific capacity of 873 mAh g^{-1}, and a peak power density of 65 mW cm^{-2}, with excellent ORR-OER cycling stability. Transition-metal chalcogenides, Co9S8 have been embedded with N, S-doped Gp-based heterostructure materials, and MWCNTs through hydrothermal reaction followed by the calcination method for the application of ORR-OER energy storage systems [154]. The prepared material exhibited an onset potential of 0.946 V (vs. RHE) in an alkaline medium and the electrode activity of ($\Delta E = E_{OER,10} - E_{ORR,1/2}$ of 890 mV). Qin et al. [155] synthesized nanocomposites of porous titanium-metal organic frameworks and N-doped Gp (Ti-MOFs/NG). The Ti-MOFs/NG composite exhibited 1.14 V and 17.84 mV dec^{-1} in 0.1 M $HClO_4$ as onset potential (E_0) and the Tafel slope, respectively, whereas relative current density was found as 99.88% of the original value after 10,800/s measurements in 0.1 M KOH. These values indicate favorable characteristics of Ti-MOFs/NG composite for ORR. In a comparative study of pyridinic-N, pyrrolic-N, graphitic-N, and pyridinic N^+-O^-, it has been found that pyridinic-N-dominated doped Gp (NDGs-800) exhibited excellent energy storage and electrocatalysis characteristics compared to others [156]. The performance of the rechargeable Zn air battery based on NDGs-800 was compared with a reference battery based on mixture of Pt/C + Ir/C (1:1 by weight) catalysts as shown in Figure 15e. The NDGs-800 based electrode shows a discharge–charge overpotential of 0.76 V at a 10 mA cm^{-2}, slightly larger than that of Pt/C + Ir/C (0.68 V), suggesting good reversibility of the rechargeable Zn-air batteries. Further, the cyclic performance is shown in Figure 15f where the voltage difference was retained for more than 78 h (up to 234 cycles) when cycled at 10 mA cm^{-2} (20 min per cycle) that was much improved compared to Pt/C + Ir/C. The feasibility of the Zn-air battery was practically demonstrated where two serially connected cells with a OCV ≈3 V were able to glow an LED as shown in Figure 15g.

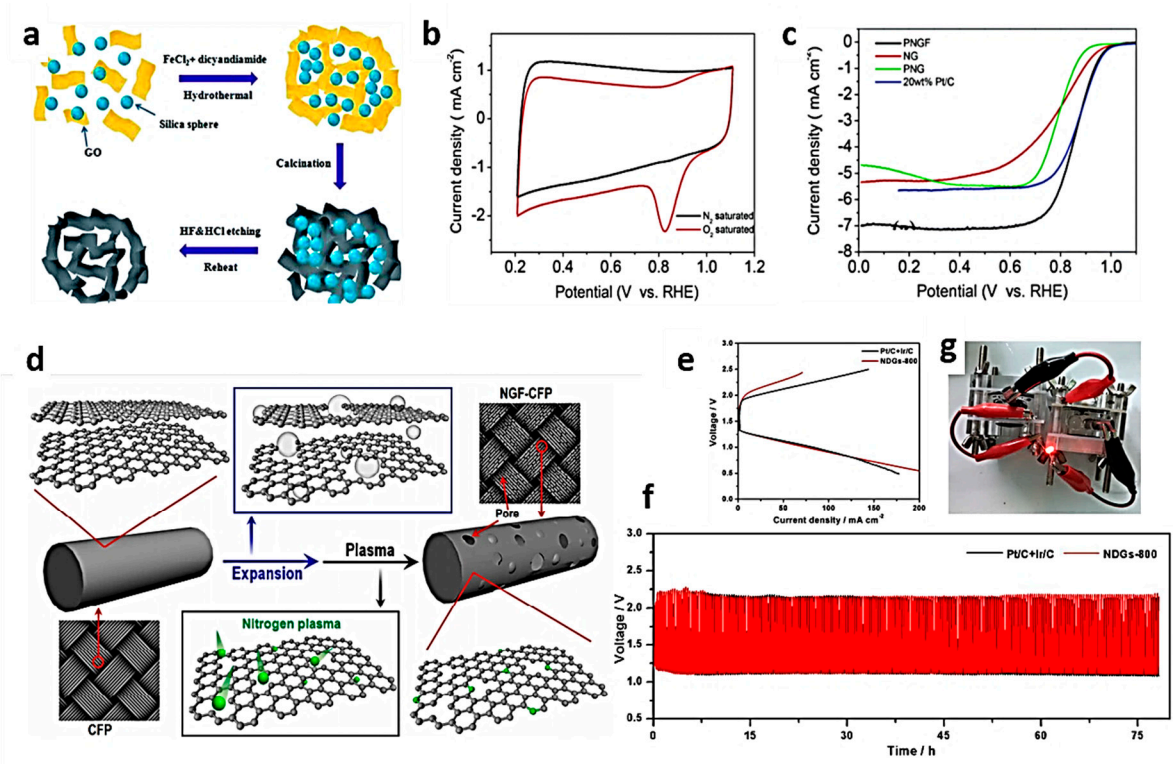

Figure 15. (**a**) Schematic representation of the synthesis procedure of PNGFs; (**b**) CV of PNGFs in 0.1 M KOH saturated with either N_2 or O_2; (**c**) LSVs of various electrocatalysts on a rotating disk electrode in 0.1 M KOH saturated with O_2; (**d**) Schematic presentation for synthesizing NGF-CFP through a facile two-step route, i.e., electrochemical expansion and nitrogen plasma treatment (**e**) Voltage profiles for the Zn-air batteries; (**f**) cycling performance at 10 mA cm^{-2}; (**g**) Two serially connected Zn-air cell glowing an LED (≈3.0 V). Reprinted with permission from [151], Copyright ACS Publishers, 2017.

Apart from using Gp derivatives as electrode for Li-air batteries, the technology of fabrication of various electrolyte materials, which may be non-aqueous, hybrid, or solid state electrode materials also play an important role in enhancing their efficiency [157]. Various fabrication techniques have been used in this consideration which are discussed extensively in literature [158,159].

5. Conclusions

In summary, this review presents the impact of N-doped Gp-derived carbon for rechargeable lithium-ion, Li-S, and Metal-Air batteries. Realizing the impact of N-doping, different reliable routes of Gp synthesis techniques are summarized to emphasize the impact of Gp-based materials for energy storage applications. The mechanically robust, highly conductive, and promising architectural design of Gp is vital for improving the electrochemical performances of various energy storage devices including Li-ion, Li-S, and Metal-Air batteries. Advanced techniques that are important for the in-depth characterization of Gp-derived materials have been briefly discussed. Substantial achievements have been reported through Gp-doped materials for such applications. Besides, the presence of different functional groups associated with Gp sheets has been proved as active materials in Li-S and Lithium-air batteries. Additionally, advanced computational studies would help in a better understanding of complex chemical/electrochemical processes happening in Gp based energy technologies. Moreover, the role of such Gp-doped materials should be extensively studied related to binders, electrodes, electrolytes, and separators. Apart from cathodes, the Gp-derivatives significantly lower the intermediate polysulfide shuttle effect. It has also shown that N-doped Gp in Li anodes prevents impulsive degradation.

To enhance the scale-up production of Li-ion batteries, sulfur utilization, sulfur loadings, energy capacity, electrolyte ratio, and the cost is still an ongoing challenge crossroad of the current era. The functionalization of Gp has entailed a vital role in rechargeable batteries to amend the efficacy of sulfur loadings. Consequently, notable progress is required for the quantitative analysis of these loadings and Gp functional doping. Chemometric studies of sulfur loadings and functional groups of graphenaceous materials should be done to optimize ratio and reduce the cost. Novel strategies should expand for the high performance of lithium batteries to overcome the impediments of their scale-up production.

As a promising emergence of recent times, challenges such as fading capacity, operational costs, and instability are still there which requires improvements among these energy storage devices.

Author Contributions: R.I., B.M.J., V.M.P., G.K.; original draft preparation, R.I., S.A.P., W.A., M.R., G.K.; review and editing, R.B., S.A.P., W.A.; formatting and graphics, G.K., B.M.J., R.I.; funding acquisition. All authors have read and agreed to the published version of the manuscript.

Funding: This work by supported by Malaysia–Thailand Joint Authority under grant number IF062-2019 and Fundamental Research Grant Scheme FP050-2019A from the University of Malaya for providing funds during the course of this study. This work was co-financed by the European Union and Greek national funds through the Operational Program Competitiveness, Entrepreneurship and Innovation, under the call RESEARCH–CREATE–INNOVATE (acronym: POLYSHIELD; project code: T1EDK-02784).

Acknowledgments: Special thanks to Shaukat Mazari (Dawood University of Engineering and Technology) for his assistance during the course of this work.

Conflicts of Interest: The authors declare that there are no conflicts of interest regarding the publication of this manuscript.

References

1. Jakob, M.; Hilaire, J. Climate science: Unburnable fossil-fuel reserves. *Nature* **2015**, *517*, 150–152. [CrossRef]
2. Nunes, L.; Causer, T.; Ciolkosz, D. Biomass for energy: A review on supply chain management models. *Renew. Sustain. Energy Rev.* **2020**, *120*, 109658. [CrossRef]
3. Jang, Y.; Kim, S.M.; Spinks, G.M.; Kim, S.J. Carbon Nanotube Yarn for Fiber-Shaped Electrical Sensors, Actuators, and Energy Storage for Smart Systems. *Adv. Mater.* **2020**, *32*, 1902670. [CrossRef] [PubMed]
4. Chu, S.; Cui, Y.; Liu, N. The path towards sustainable energy. *Nat. Mater.* **2017**, *16*, 16–22. [CrossRef] [PubMed]
5. Xia, F.; Mueller, T.; Lin, Y.-M.; Valdes-Garcia, A.; Avouris, P. Ultrafast graphene photodetector. *Nat. Nanotechnol.* **2009**, *4*, 839. [CrossRef]
6. Gao, W.; Alemany, L.B.; Ci, L.; Ajayan, P.M. New insights into the structure and reduction of graphite oxide. *Nat. Chem.* **2009**, *1*, 403. [CrossRef]
7. Wei, L.; Zhao, T.; Zhao, G.; An, L.; Zeng, L. A high-performance carbon nanoparticle-decorated graphite felt electrode for vanadium redox flow batteries. *Appl. Energy* **2016**, *176*, 74–79. [CrossRef]
8. Kim, H.; Miura, Y.; Macosko, C.W. Graphene/polyurethane nanocomposites for improved gas barrier and electrical conductivity. *Chem. Mater.* **2010**, *22*, 3441–3450. [CrossRef]
9. Suk, J.W.; Piner, R.D.; An, J.; Ruoff, R.S. Mechanical properties of monolayer graphene oxide. *ACS Nano* **2010**, *4*, 6557–6564. [CrossRef]
10. Mariyappan, S.; Marchandier, T.; Rabuel, F.; Iadecola, A.; Rousse, G.; Morozov, A.V.; Abakumov, A.M.; Tarascon, J.-M. The role of divalent (Zn^{2+}/Mg^{2+}/Cu^{2+}) substituents in achieving full capacity of sodium layered oxides for Na-ion battery applications. *Chem. Mater.* **2020**, *32*, 1657–1666. [CrossRef]
11. Osada, I.; de Vries, H.; Scrosati, B.; Passerini, S. Ionic-liquid-based polymer electrolytes for battery applications. *Angew. Chem. Int. Ed.* **2016**, *55*, 500–513. [CrossRef] [PubMed]
12. Yahia, M.B.; Vergnet, J.; Saubanère, M.; Doublet, M.-L. Unified picture of anionic redox in Li/Na-ion batteries. *Nat. Mater.* **2019**, *18*, 496–502. [CrossRef] [PubMed]
13. Pervez, S.A.; Kim, D.; Lee, S.M.; Doh, C.H.; Lee, S.; Farooq, U.; Saleem, M. Study of tin-sulphur-carbon nanocomposites based on electrically exploded tin as anode for sodium battery. *J. Power Sources* **2016**, *315*, 218–223. [CrossRef]

14. Kaveevivitchai, W.; Manthiram, A. High-capacity zinc-ion storage in an open-tunnel oxide for aqueous and nonaqueous Zn-ion batteries. *J. Mater. Chem. A* **2016**, *4*, 18737–18741. [CrossRef]
15. Jayaprakash, N.; Shen, J.; Moganty, S.S.; Corona, A.; Archer, L.A. Porous hollow carbon@ sulfur composites for high-power lithium–sulfur batteries. *Angew. Chem. Int. Ed.* **2011**, *50*, 5904–5908. [CrossRef] [PubMed]
16. Pervez, S.A.; Vinayan, B.P.; Cambaz, M.A.; Melinte, G.; Diemant, T.; Braun, T.; Karkera, G.; Behm, R.J.; Fichtner, M. Electrochemical and compositional characterization of solid interphase layers in an interface-modified solid-state Li–sulfur battery. *J. Mater. Chem. A* **2020**, *8*, 16451–16462. [CrossRef]
17. Jian, Z.; Luo, W.; Ji, X. Carbon electrodes for K-ion batteries. *J. Am. Chem. Soc.* **2015**, *137*, 11566–11569. [CrossRef]
18. Armand, M.; Tarascon, J.-M. Building better batteries. *Nature* **2008**, *451*, 652–657. [CrossRef]
19. Geim, A.K.; Novoselov, K.S. The rise of graphene. In *Nanoscience and Technology: A Collection of Reviews from Nature Journals*; World Scientific: London, UK, 2010; pp. 11–19.
20. Du, J.; Pei, S.; Ma, L.; Cheng, H.M. 25th anniversary article: Carbon nanotube-and graphene-based transparent conductive films for optoelectronic devices. *Adv. Mater.* **2014**, *26*, 1958–1991. [CrossRef]
21. Jang, S.; Hwang, E.; Lee, Y.; Lee, S.; Cho, J.H. Multifunctional graphene optoelectronic devices capable of detecting and storing photonic signals. *Nano Lett.* **2015**, *15*, 2542–2547. [CrossRef]
22. Polat, E.O.; Balci, O.; Kakenov, N.; Uzlu, H.B.; Kocabas, C.; Dahiya, R. Synthesis of large area graphene for high performance in flexible optoelectronic devices. *Sci. Rep.* **2015**, *5*, 16744. [CrossRef] [PubMed]
23. Xu, H.; Chen, H.; Lai, H.; Li, Z.; Dong, X.; Cai, S.; Chu, X.; Gao, C. Capacitive charge storage enables an ultrahigh cathode capacity in aluminum-graphene battery. *J. Energy Chem.* **2020**, *45*, 40–44. [CrossRef]
24. Simanjuntak, C.; Siburian, R.; Marpaung, H. Properties of Mg/graphite and Mg/graphene as cathode electrode on primary cell battery. *Heliyon* **2020**, *6*, e03118. [CrossRef] [PubMed]
25. Zhang, J.; Zhang, X.; Hou, Z.; Zhang, L.; Li, C. Uniform SiOx/graphene composite materials for lithium ion battery anodes. *J. Alloys Compd.* **2019**, *809*, 151798. [CrossRef]
26. Yang, X.; Qiu, J.; Liu, M.; Ming, H.; Zhang, H.; Li, M.; Zhang, S.; Zhang, T. A surface multiple effect on the ZnO anode induced by graphene for a high energy lithium-ion full battery. *J. Alloys Compd.* **2020**, *824*, 153945. [CrossRef]
27. Mukherjee, S.; Kavalsky, L.; Chattopadhyay, K.; Singh, C.V. Dramatic improvement in the performance of graphene as Li/Na battery anodes with suitable electrolytic solvents. *Carbon* **2020**, *161*, 570–576. [CrossRef]
28. Yue, L.; Jayapal, M.; Cheng, X.; Zhang, T.; Chen, J.; Ma, X.; Dai, X.; Lu, H.; Guan, R.; Zhang, W. Highly dispersed ultra-small nano Sn-SnSb nanoparticles anchored on N-doped graphene sheets as high performance anode for sodium ion batteries. *Appl. Surf. Sci.* **2020**, *512*, 145686. [CrossRef]
29. Dada, O.J. Higher capacity utilization and rate performance of lead acid battery electrodes using graphene additives. *J. Energy Storage* **2019**, *23*, 579–589. [CrossRef]
30. Luan, Y.; Yin, J.; Zhu, K.; Cheng, K.; Yan, J.; Ye, K.; Wang, G.; Cao, D. Arc-discharge production of high-quality fluorine-modified graphene as anode for Li-ion battery. *Chem. Eng. J.* **2019**, *392*, 123668. [CrossRef]
31. Na, R.; Liu, Y.; Wu, Z.-P.; Cheng, X.; Shan, Z.; Zhong, C.-J.; Tian, J. Nano-Silicon composite materials with N-doped graphene of controllable and optimal pyridinic-to-pyrrolic structural ratios for lithium ion battery. *Electrochim. Acta* **2019**, *321*, 134742. [CrossRef]
32. Lang, B. A LEED study of the deposition of carbon on platinum crystal surfaces. *Surf. Sci.* **1975**, *53*, 317–329. [CrossRef]
33. Ajayan, P.; Nugent, J.; Siegel, R.; Wei, B.; Kohler-Redlich, P. Growth of carbon micro-trees. *Nature* **2000**, *404*, 243. [CrossRef] [PubMed]
34. Novoselov, K.S.; Geim, A.K.; Morozov, S.; Dubonos, S.; Zhang, Y.; Jiang, D. Room-temperature electric field effect and carrier-type inversion in graphene films. *arXiv* **2004**, arXiv:cond-mat/0410631.
35. Yi, M.; Shen, Z. A review on mechanical exfoliation for the scalable production of graphene. *J. Mater. Chem. A* **2015**, *3*, 11700–11715. [CrossRef]
36. Zhang, L.; Li, X.; Huang, Y.; Ma, Y.; Wan, X.; Chen, Y. Controlled synthesis of few-layered graphene sheets on a large scale using chemical exfoliation. *Carbon* **2010**, *48*, 2367–2371. [CrossRef]
37. Park, J.-U.; Nam, S.; Lee, M.-S.; Lieber, C.M. Synthesis of monolithic graphene–graphite integrated electronics. *Nat. Mater.* **2012**, *11*, 120. [CrossRef] [PubMed]

38. Sharif, F.; Zeraati, A.S.; Ganjeh-Anzabi, P.; Yasri, N.; Perez-Page, M.; Holmes, S.M.; Sundararaj, U.; Trifkovic, M.; Roberts, E.P.L. Synthesis of a high-temperature stable electrochemically exfoliated graphene. *Carbon* **2020**, *157*, 681–692. [CrossRef]
39. Obraztsov, A.N. Chemical vapour deposition: Making graphene on a large scale. *Nat. Nanotechnol.* **2009**, *4*, 212. [CrossRef]
40. Kosynkin, D.V.; Higginbotham, A.L.; Sinitskii, A.; Lomeda, J.R.; Dimiev, A.; Price, B.K.; Tour, J.M. Longitudinal unzipping of carbon nanotubes to form graphene nanoribbons. *Nature* **2009**, *458*, 872–876. [CrossRef]
41. Wu, W.; Liu, M.; Gu, Y.; Guo, B.; Ma, H.; Wang, P.; Wang, X.; Zhang, R. Fast chemical exfoliation of graphite to few-layer graphene with high quality and large size via a two-step microwave-assisted process. *Chem. Eng. J.* **2020**, *381*, 122592. [CrossRef]
42. Tsyganov, D.; Bundaleska, N.; Dias, A.; Henriques, J.; Felizardo, E.; Abrashev, M.; Kissovski, J.; do Rego, A.B.; Ferraria, A.; Tatarova, E. Microwave plasma-based direct synthesis of free-standing N-graphene. *Phys. Chem. Chem. Phys.* **2020**, *22*, 4772–4787. [CrossRef] [PubMed]
43. Lockett, M.; Sarmiento, V.; Balingit, M.; Oropeza-Guzmán, M.T.; Vázquez-Mena, O. Direct chemical conversion of continuous CVD graphene/graphite films to graphene oxide without exfoliation. *Carbon* **2020**, *158*, 202–209. [CrossRef]
44. Lee, S.; Park, W.K.; Yoon, Y.; Baek, B.; Yoo, J.S.; Kwon, S.B.; Kim, D.H.; Hong, Y.J.; Kang, B.K.; Yoon, D.H. Quality improvement of fast-synthesized graphene films by rapid thermal chemical vapor deposition for mass production. *Mater. Sci. Eng. B* **2019**, *242*, 63–68. [CrossRef]
45. Li, M.; Liu, D.; Wei, D.; Song, X.; Wei, D.; Wee, A.T.S. Controllable synthesis of graphene by plasma-enhanced chemical vapor deposition and its related applications. *Adv. Sci.* **2016**, *3*, 1600003. [CrossRef] [PubMed]
46. Shiraz, H.G.; Tavakoli, O. Investigation of graphene-based systems for hydrogen storage. *Renew. Sustain. Energy Rev.* **2017**, *74*, 104–109. [CrossRef]
47. Petnikota, S.; Rotte, N.K.; Srikanth, V.V.; Kota, B.S.; Reddy, M.; Loh, K.P.; Chowdari, B. Electrochemical studies of few-layered graphene as an anode material for Li ion batteries. *J. Solid State Electrochem.* **2014**, *18*, 941–949. [CrossRef]
48. Petnikota, S.; Rotte, N.K.; Reddy, M.V.; Srikanth, V.V.S.S.; Chowdari, B.V.R. MgO-Decorated Few-Layered Graphene as an Anode for Li-Ion Batteries. *ACS Appl. Mater. Interfaces* **2015**, *7*, 2301–2309. [CrossRef]
49. Goh, B.-M.; Wang, Y.; Reddy, M.; Ding, Y.L.; Lu, L.; Bunker, C.; Loh, K.P. Filling the voids of graphene foam with graphene "eggshell" for improved lithium-ion storage. *ACS Appl. Mater. Interfaces* **2014**, *6*, 9835–9841. [CrossRef]
50. Tsang, C.H.A.; Huang, H.; Xuan, J.; Wang, H.; Leung, D. Graphene materials in green energy applications: Recent development and future perspective. *Renew. Sustain. Energy Rev.* **2020**, *120*, 109656. [CrossRef]
51. Kruskopf, M.; Pakdehi, D.M.; Pierz, K.; Wundrack, S.; Stosch, R.; Dziomba, T.; Götz, M.; Baringhaus, J.; Aprojanz, J.; Tegenkamp, C. Comeback of epitaxial graphene for electronics: Large-area growth of bilayer-free graphene on SiC. *2D Materials* **2016**, *3*, 041002. [CrossRef]
52. Zhang, Y.; Ma, Q.; Wang, S.; Liu, X.; Li, L. Poly(vinyl alcohol)-Assisted Fabrication of Hollow Carbon Spheres/Reduced Graphene Oxide Nanocomposites for High-Performance Lithium-Ion Battery Anodes. *ACS Nano* **2018**, *12*, 4824–4834. [CrossRef] [PubMed]
53. Nanda, S.S.; Kim, M.J.; Yeom, K.S.; An, S.S.A.; Ju, H.; Yi, D.K. Raman spectrum of graphene with its versatile future perspectives. *TrAC Trends Anal. Chem.* **2016**, *80*, 125–131. [CrossRef]
54. Wu, J.-B.; Lin, M.-L.; Cong, X.; Liu, H.-N.; Tan, P.-H. Raman spectroscopy of graphene-based materials and its applications in related devices. *Chem. Soc. Rev.* **2018**, *47*, 1822–1873. [CrossRef] [PubMed]
55. Zabel, J.; Nair, R.R.; Ott, A.; Georgiou, T.; Geim, A.K.; Novoselov, K.S.; Casiraghi, C. Raman spectroscopy of graphene and bilayer under biaxial strain: Bubbles and balloons. *Nano Lett.* **2012**, *12*, 617–621. [CrossRef]
56. Han, C.; Zhang, H.; Zhang, D.; Deng, Y.; Shen, J.; Zeng, G. Ultrafine FeNi3 Nanocrystals Embedded in 3D Honeycomb-Like Carbon Matrix for High-Performance Microwave Absorption. *Nanomaterials* **2020**, *10*, 598. [CrossRef]
57. Chen, J.; Dai, Y.; Ma, Y.; Dai, X.; Ho, W.; Xie, M. Ultrathin β-tellurium layers grown on highly oriented pyrolytic graphite by molecular-beam epitaxy. *Nanoscale* **2017**, *9*, 15945–15948. [CrossRef]
58. Casimir, D.; Alghamdi, H.; Ahmed, I.Y.; Garcia-Sanchez, R.; Misra, P. Raman Spectroscopy of Graphene, Graphite and Graphene Nanoplatelets. In *2D Materials*; IntechOpen: London, UK, 2019.

59. Ye, X.; Zhou, Q.; Jia, C.; Tang, Z.; Zhu, Y.; Wan, Z. Producing large-area, foldable graphene paper from graphite oxide suspensions by in-situ chemical reduction process. *Carbon* **2017**, *114*, 424–434. [CrossRef]
60. Lee, H.C.; Liu, W.-W.; Chai, S.-P.; Mohamed, A.R.; Aziz, A.; Khe, C.-S.; Hidayah, N.M.; Hashim, U. Review of the synthesis, transfer, characterization and growth mechanisms of single and multilayer graphene. *RSC Adv.* **2017**, *7*, 15644–15693. [CrossRef]
61. Yoon, D.; Cheong, H. Raman spectroscopy for characterization of graphene. In *Raman Spectroscopy for Nanomaterials Characterization*; Springer: Berlin/Heidelberg, Germany, 2012; pp. 191–214.
62. Luo, L.; Wu, J.; Luo, J.; Huang, J.; Dravid, V.P. Dynamics of electrochemical lithiation/delithiation of graphene-encapsulated silicon nanoparticles studied by in-situ TEM. *Sci. Rep.* **2014**, *4*, 1–7. [CrossRef]
63. Allen, M.J.; Tung, V.C.; Kaner, R.B. Honeycomb carbon: A review of graphene. *Chem. Rev.* **2010**, *110*, 132–145. [CrossRef]
64. Kumar, R.; Singh, R.K.; Singh, D.P. Natural and waste hydrocarbon precursors for the synthesis of carbon based nanomaterials: Graphene and CNTs. *Renew. Sustain. Energy Rev.* **2016**, *58*, 976–1006. [CrossRef]
65. Lo, K.S.K.; Leung, W.W.F. Dye-sensitized solar cells with shear-exfoliated graphene. *Sol. Energy* **2019**, *180*, 16–24. [CrossRef]
66. Cao, N.; Zhang, Y. Study of reduced graphene oxide preparation by Hummers' method and related characterization. *J. Nanomater.* **2015**, *2015*, 168125. [CrossRef]
67. Van Khai, T.; Kwak, D.S.; Kwon, Y.J.; Cho, H.Y.; Huan, T.N.; Chung, H.; Ham, H.; Lee, C.; Van Dan, N.; Tung, N.T. Direct production of highly conductive graphene with a low oxygen content by a microwave-assisted solvothermal method. *Chem. Eng. J.* **2013**, *232*, 346–355. [CrossRef]
68. Gui, Y.; Yuan, J.; Wang, W.; Zhao, J.; Tian, J.; Xie, B. Facile solvothermal synthesis and gas sensitivity of graphene/WO3 nanocomposites. *Materials* **2014**, *7*, 4587–4600. [CrossRef]
69. Meng, L.; Li, Y.; Liu, T.S.; Zhu, C.; Li, Q.Y.; Chen, X.; Zhang, S.; Zhang, X.; Bao, L.; Huang, Y.; et al. Wrinkle networks in exfoliated multilayer graphene and other layered materials. *Carbon* **2020**, *156*, 24–30. [CrossRef]
70. Hawaldar, R.; Merino, P.; Correia, M.R.; Bdikin, I.; Grácio, J.; Méndez, J.; Martín-Gago, J.A.; Singh, M.K. Large-area high-throughput synthesis of monolayer graphene sheet by Hot Filament Thermal Chemical Vapor Deposition. *Sci. Rep.* **2012**, *2*, 682. [CrossRef]
71. Dang, C.; Che, Q.L.; Gao, B.L.; Li, L.; Wang, B.B. Growth, photoluminescence and thermal conductance of graphene-like nanoflakes grown on copper foils in methane environment. *Mater. Sci. Semicond. Process.* **2014**, *27*, 97–102. [CrossRef]
72. Tu, Z.; Liu, Z.; Li, Y.; Yang, F.; Zhang, L.; Zhao, Z.; Xu, C.; Wu, S.; Liu, H.; Yang, H.; et al. Controllable growth of 1–7 layers of graphene by chemical vapour deposition. *Carbon* **2014**, *73*, 252–258. [CrossRef]
73. Martin-Olmos, C.; Rasool, H.I.; Weiller, B.H.; Gimzewski, J.K. Graphene MEMS: AFM Probe Performance Improvement. *ACS Nano* **2013**, *7*, 4164–4170. [CrossRef] [PubMed]
74. Lui, C.H.; Liu, L.; Mak, K.F.; Flynn, G.W.; Heinz, T.F. Ultraflat graphene. *Nature* **2009**, *462*, 339–341. [CrossRef] [PubMed]
75. Gao, J.-H.; Ishida, N.; Scott, I.; Fujita, D. Controllable growth of single-layer graphene on a Pd(111) substrate. *Carbon* **2012**, *50*, 1674–1680. [CrossRef]
76. Liu, C.; Hu, G.; Gao, H. Preparation of few-layer and single-layer graphene by exfoliation of expandable graphite in supercritical N,N-dimethylformamide. *J. Supercrit. Fluids* **2012**, *63*, 99–104. [CrossRef]
77. Mehrali, M.; Latibari, S.T.; Mehrali, M.; Indra Mahlia, T.M.; Cornelis Metselaar, H.S. Preparation and properties of highly conductive palmitic acid/graphene oxide composites as thermal energy storage materials. *Energy* **2013**, *58*, 628–634. [CrossRef]
78. Pool, V.L.; Dou, B.; Van Campen, D.G.; Klein-Stockert, T.R.; Barnes, F.S.; Shaheen, S.E.; Ahmad, M.I.; van Hest, M.F.A.M.; Toney, M.F. Thermal engineering of FAPbI3 perovskite material via radiative thermal annealing and in situ XRD. *Nat. Commun.* **2017**, *8*, 14075. [CrossRef] [PubMed]
79. Naebe, M.; Wang, J.; Amini, A.; Khayyam, H.; Hameed, N.; Li, L.H.; Chen, Y.; Fox, B. Mechanical Property and Structure of Covalent Functionalised Graphene/Epoxy Nanocomposites. *Sci. Rep.* **2014**, *4*, 4375. [CrossRef]
80. Wu, J.; Pan, Z.; Zhang, Y.; Wang, B.; Peng, H. The recent progress of nitrogen-doped carbon nanomaterials for electrochemical batteries. *J. Mater. Chem. A* **2018**, *6*, 12932–12944. [CrossRef]
81. Rana, M.; Luo, B.; Kaiser, M.R.; Gentle, I.; Knibbe, R. The role of functional materials to produce high areal capacity lithium sulfur battery. *J. Energy Chem.* **2019**, *42*, 195–209. [CrossRef]

82. Sui, Z.-Y.; Wang, C.; Yang, Q.-S.; Shu, K.; Liu, Y.-W.; Han, B.-H.; Wallace, G.G. A highly nitrogen-doped porous graphene—An anode material for lithium ion batteries. *J. Mater. Chem. A* **2015**, *3*, 18229–18237. [CrossRef]
83. Armstrong, A.R.; Bruce, P.G. Synthesis of layered LiMnO2 as an electrode for rechargeable lithium batteries. *Nature* **1996**, *381*, 499–500. [CrossRef]
84. Reddy, A.L.M.; Srivastava, A.; Gowda, S.R.; Gullapalli, H.; Dubey, M.; Ajayan, P.M. Synthesis of nitrogen-doped graphene films for lithium battery application. *ACS Nano* **2010**, *4*, 6337–6342. [CrossRef]
85. Liu, X.; Zhang, J.; Guo, S.; Pinna, N. Graphene/N-doped carbon sandwiched nanosheets with ultrahigh nitrogen doping for boosting lithium-ion batteries. *J. Mater. Chem. A* **2016**, *4*, 1423–1431. [CrossRef]
86. Bulusheva, L.G.; Okotrub, A.V.; Kurenya, A.G.; Zhang, H.; Zhang, H.; Chen, X.; Song, H. Electrochemical properties of nitrogen-doped carbon nanotube anode in Li-ion batteries. *Carbon* **2011**, *49*, 4013–4023. [CrossRef]
87. Zhou, X.; Wan, L.-J.; Guo, Y.-G. Binding SnO2 Nanocrystals in Nitrogen-Doped Graphene Sheets as Anode Materials for Lithium-Ion Batteries. *Adv. Mater.* **2013**, *25*, 2152–2157. [CrossRef] [PubMed]
88. Faisal, S.N.; Subramaniyam, C.M.; Haque, E.; Islam, M.M.; Noorbehesht, N.; Roy, A.K.; Islam, M.S.; Liu, H.K.; Dou, S.X.; Harris, A.T.; et al. Nanoarchitectured Nitrogen-Doped Graphene/Carbon Nanotube as High Performance Electrodes for Solid State Supercapacitors, Capacitive Deionization, Li-Ion Battery, and Metal-Free Bifunctional Electrocatalysis. *ACS Appl. Energy Mater.* **2018**, *1*, 5211–5223. [CrossRef]
89. Puttapati, S.K.; Gedela, V.; Srikanth, V.V.; Reddy, M.; Adams, S.; Chowdari, B. Unique reduced graphene oxide as efficient anode material in Li ion battery. *Bull. Mater. Sci.* **2018**, *41*, 53. [CrossRef]
90. Fang, R.; Chen, K.; Yin, L.; Sun, Z.; Li, F.; Cheng, H.M. The regulating role of carbon nanotubes and graphene in lithium-ion and lithium–sulfur batteries. *Adv. Mater.* **2019**, *31*, 1800863. [CrossRef] [PubMed]
91. Wu, F.; Maier, J.; Yu, Y. Guidelines and trends for next-generation rechargeable lithium and lithium-ion batteries. *Chem. Soc. Rev.* **2020**, *49*, 1569–1614. [CrossRef]
92. Qu, L.; Liu, P.; Yi, Y.; Wang, T.; Yang, P.; Tian, X.; Li, M.; Yang, B.; Dai, S. Enhanced Cycling Performance for Lithium–Sulfur Batteries by a Laminated 2D g-C3N4/Graphene Cathode Interlayer. *ChemSusChem* **2019**, *12*, 213–223. [CrossRef]
93. Jin, J.; Cai, W.; Cai, J.; Shao, Y.; Song, Y.; Xia, Z.; Zhang, Q.; Sun, J. MOF-derived hierarchical CoP nanoflakes anchored on vertically erected graphene scaffolds as self-supported and flexible hosts for lithium–sulfur batteries. *J. Mater. Chem. A* **2020**, *8*, 3027–3034. [CrossRef]
94. Chiochan, P.; Kosasang, S.; Ma, N.; Duangdangchote, S.; Suktha, P.; Sawangphruk, M. Confining Li2S6 catholyte in 3D graphene sponge with ultrahigh total pore volume and oxygen-containing groups for lithium-sulfur batteries. *Carbon* **2020**, *158*, 244–255. [CrossRef]
95. Lu, L.; Pei, F.; Abeln, T.; Pei, Y. Tailoring three-dimensional interconnected nanoporous graphene micro/nano-foams for lithium-sulfur batteries. *Carbon* **2020**, *157*, 437–447. [CrossRef]
96. Xiao, S.; Zhang, J.; Deng, Y.; Zhou, G.; Wang, R.; He, Y.-B.; Lv, W.; Yang, Q.-H. Graphene-Templated Growth of WS2 Nanoclusters for Catalytic Conversion of Polysulfides in Lithium–Sulfur Batteries. *ACS Appl. Energy Mater.* **2020**, *3*, 4923–4930. [CrossRef]
97. Liu, G.; Zhang, Z.; Tian, W.; Chen, W.; Xi, B.; Li, H.; Feng, J.; Xiong, S. Ni12P5 nanoparticles bound on graphene sheets for advanced lithium–sulfur batteries. *Nanoscale* **2020**, *12*, 10760–10770. [CrossRef]
98. Hu, Y.; Chen, W.; Lei, T.; Jiao, Y.; Wang, H.; Wang, X.; Rao, G.; Wang, X.; Chen, B.; Xiong, J. Graphene quantum dots as the nucleation sites and interfacial regulator to suppress lithium dendrites for high-loading lithium-sulfur battery. *Nano Energy* **2020**, *68*, 104373. [CrossRef]
99. Wang, B.; Jin, F.; Xie, Y.; Luo, H.; Wang, F.; Ruan, T.; Wang, D.; Zhou, Y.; Dou, S. Holey graphene modified LiFePO4 hollow microsphere as an efficient binary sulfur host for high-performance lithium-sulfur batteries. *Energy Storage Mater.* **2020**, *26*, 433–442. [CrossRef]
100. Fang, R.; Zhao, S.; Sun, Z.; Wang, D.-W.; Cheng, H.-M.; Li, F. More Reliable Lithium-Sulfur Batteries: Status, Solutions and Prospects. *Adv. Mater.* **2017**, *29*, 1606823. [CrossRef]
101. Guo, J.; Xu, Y.; Wang, C. Sulfur-Impregnated Disordered Carbon Nanotubes Cathode for Lithium–Sulfur Batteries. *Nano Lett.* **2011**, *11*, 4288–4294. [CrossRef]
102. Song, J.; Gordin, M.L.; Xu, T.; Chen, S.; Yu, Z.; Sohn, H.; Lu, J.; Ren, Y.; Duan, Y.; Wang, D. Strong Lithium Polysulfide Chemisorption on Electroactive Sites of Nitrogen-Doped Carbon Composites For High-Performance Lithium–Sulfur Battery Cathodes. *Angew. Chem. Int. Ed.* **2015**, *54*, 4325–4329. [CrossRef]

103. Wen, X.; Xiang, K.; Zhu, Y.; Xiao, L.; Liao, H.; Chen, W.; Chen, X.; Chen, H. 3D hierarchical nitrogen-doped graphene/CNTs microspheres as a sulfur host for high-performance lithium-sulfur batteries. *J. Alloys Compd.* **2020**, *815*, 152350. [CrossRef]
104. Li, H.; Liu, D.; Zhu, X.; Qu, D.; Xie, Z.; Li, J.; Tang, H.; Zheng, D.; Qu, D. Integrated 3D electrodes based on metal-nitrogen-doped graphitic ordered mesoporous carbon and carbon paper for high-loading lithium-sulfur batteries. *Nano Energy* **2020**, *73*, 104763. [CrossRef]
105. Cheng, D.; Wu, P.; Wang, J.; Tang, X.; An, T.; Zhou, H.; Zhang, D.; Fan, T. Synergetic pore structure optimization and nitrogen doping of 3D porous graphene for high performance lithium sulfur battery. *Carbon* **2019**, *143*, 869–877. [CrossRef]
106. Du, Z.; Chen, X.; Hu, W.; Chuang, C.; Xie, S.; Hu, A.; Yan, W.; Kong, X.; Wu, X.; Ji, H. Cobalt in nitrogen-doped graphene as single-atom catalyst for high-sulfur content lithium–sulfur batteries. *J. Am. Chem. Soc.* **2019**, *141*, 3977–3985. [CrossRef] [PubMed]
107. Wang, C.; Su, K.; Wan, W.; Guo, H.; Zhou, H.; Chen, J.; Zhang, X.; Huang, Y. High sulfur loading composite wrapped by 3D nitrogen-doped graphene as a cathode material for lithium–sulfur batteries. *J. Mater. Chem. A* **2014**, *2*, 5018–5023. [CrossRef]
108. Tang, C.; Zhang, Q.; Zhao, M.-Q.; Huang, J.-Q.; Cheng, X.-B.; Tian, G.-L.; Peng, H.-J.; Wei, F. Nitrogen-Doped Aligned Carbon Nanotube/Graphene Sandwiches: Facile Catalytic Growth on Bifunctional Natural Catalysts and Their Applications as Scaffolds for High-Rate Lithium-Sulfur Batteries. *Adv. Mater.* **2014**, *26*, 6100–6105. [CrossRef] [PubMed]
109. Zhang, L.; Liu, D.; Muhammad, Z.; Wan, F.; Xie, W.; Wang, Y.; Song, L.; Niu, Z.; Chen, J. Single Nickel Atoms on Nitrogen-Doped Graphene Enabling Enhanced Kinetics of Lithium–Sulfur Batteries. *Adv. Mater.* **2019**, *31*, 1903955. [CrossRef] [PubMed]
110. Zuo, X.; Zhen, M.; Wang, C. Ni@N-doped graphene nanosheets and CNTs hybrids modified separator as efficient polysulfide barrier for high-performance lithium sulfur batteries. *Nano Res.* **2019**, *12*, 829–836. [CrossRef]
111. Li, F.; Liu, Q.; Hu, J.; Feng, Y.; He, P.; Ma, J. Recent advances in cathode materials for rechargeable lithium–sulfur batteries. *Nanoscale* **2019**, *11*, 15418–15439. [CrossRef]
112. Manthiram, A.; Fu, Y.; Chung, S.-H.; Zu, C.; Su, Y.-S. Rechargeable lithium–sulfur batteries. *Chem. Rev.* **2014**, *114*, 11751–11787. [CrossRef]
113. Su, D.; Zhou, D.; Wang, C.; Wang, G. Lithium-Sulfur Batteries: Toward High Performance Lithium–Sulfur Batteries Based on Li2S Cathodes and Beyond: Status, Challenges, and Perspectives (Adv. Funct. Mater. 38/2018). *Adv. Funct. Mater.* **2018**, *28*, 1870273. [CrossRef]
114. Reddy, M.V.; Mauger, A.; Julien, C.M.; Paolella, A.; Zaghib, K. Brief History of Early Lithium-Battery Development. *Materials* **2020**, *13*, 1884. [CrossRef] [PubMed]
115. Reddy, M.; Subba Rao, G.; Chowdari, B. Metal oxides and oxysalts as anode materials for Li ion batteries. *Chem. Rev.* **2013**, *113*, 5364–5457. [CrossRef] [PubMed]
116. Reddy, M.V.; Julien, C.M.; Mauger, A.; Zaghib, K. Sulfide and oxide inorganic solid electrolytes for all-solid-state Li batteries: A Review. *Nanomaterials* **2020**, *10*, 1606. [CrossRef] [PubMed]
117. Fu, A.; Wang, C.; Pei, F.; Cui, J.; Fang, X.; Zheng, N. Recent advances in hollow porous carbon materials for lithium–sulfur batteries. *Small* **2019**, *15*, 1804786. [CrossRef]
118. Zhang, L.; Wang, Y.; Niu, Z.; Chen, J. Advanced nanostructured carbon-based materials for rechargeable lithium-sulfur batteries. *Carbon* **2019**, *141*, 400–416. [CrossRef]
119. Zhu, J.; Zhu, P.; Yan, C.; Dong, X.; Zhang, X. Recent progress in polymer materials for advanced lithium-sulfur batteries. *Prog. Polym. Sci.* **2019**, *90*, 118–163. [CrossRef]
120. Ren, W.; Ma, W.; Zhang, S.; Tang, B. Recent advances in shuttle effect inhibition for lithium sulfur batteries. *Energy Storage Mater.* **2019**, *23*, 707–732. [CrossRef]
121. Wang, C.; Yi, Y.; Li, H.; Wu, P.; Li, M.; Jiang, W.; Chen, Z.; Li, H.; Zhu, W.; Dai, S. Rapid gas-assisted exfoliation promises V2O5 nanosheets for high performance lithium-sulfur batteries. *Nano Energy* **2020**, *67*, 104253. [CrossRef]
122. Zhang, S.; Xu, D.; Su, C.; Tang, W.; Ju, H.; Zhang, J.; Tian, B. Hermetically encapsulating sulfur by FePS3 flakes for high-performance lithium sulfur batteries. *Chem. Commun.* **2020**, *56*, 810–813. [CrossRef]

123. Qi, W.; Jiang, W.; Xu, F.; Jia, J.; Yang, C.; Cao, B. Improving confinement and redox kinetics of polysufides through hollow NC@ CeO2 nanospheres for high-performance lithium-sulfur batteries. *Chem. Eng. J.* **2020**, *382*, 122852. [CrossRef]
124. Chen, G.; Li, Y.; Zhong, W.; Zheng, F.; Hu, J.; Ji, X.; Liu, W.; Yang, C.; Lin, Z.; Liu, M. MOFs-derived porous Mo2C–C nano-octahedrons enable high-performance lithium–sulfur batteries. *Energy Storage Mater.* **2020**, *25*, 547–554. [CrossRef]
125. Hao, Q.; Cui, G.; Zhang, Y.; Li, J.; Zhang, Z. Novel MoSe2/MoO2 heterostructure as an effective sulfur host for high-performance lithium/sulfur batteries. *Chem. Eng. J.* **2020**, *381*, 122672. [CrossRef]
126. Chen, X.; Hou, T.; Persson, K.A.; Zhang, Q. Combining theory and experiment in lithium–sulfur batteries: Current progress and future perspectives. *Mater. Today* **2019**, *22*, 142–158. [CrossRef]
127. Zhao, Z.; Wang, J.; Cheng, M.; Wu, J.; Zhang, Q.; Liu, X.; Wang, C.; Wang, J.; Li, K.; Wang, J. N-doped porous carbon-graphene cables synthesized for self-standing cathode and anode hosts of Li–S batteries. *Electrochim. Acta* **2020**, *349*, 136231. [CrossRef]
128. Wang, D.; Liu, H.; Shan, Z.; Xia, D.; Na, R.; Liu, H.; Chen, Z.; Wang, B.; Tian, J. Nitrogen, Sulfur Co-doped Porous Graphene Boosts Li4Ti5O12 Anode Performance for High-Rate and Long-Life Lithium Ion Batteries. *Energy Storage Mater.* **2020**, *27*, 387–395. [CrossRef]
129. Wang, H.; Zhang, C.; Liu, Z.; Wang, L.; Han, P.; Xu, H.; Zhang, K.; Dong, S.; Yao, J.; Cui, G. Nitrogen-doped graphene nanosheets with excellent lithium storage properties. *J. Mater. Chem.* **2011**, *21*, 5430–5434. [CrossRef]
130. Qie, L.; Chen, W.M.; Wang, Z.H.; Shao, Q.G.; Li, X.; Yuan, L.X.; Hu, X.L.; Zhang, W.X.; Huang, Y.H. Nitrogen-doped porous carbon nanofiber webs as anodes for lithium ion batteries with a superhigh capacity and rate capability. *Adv. Mater.* **2012**, *24*, 2047–2050. [CrossRef]
131. Li, Z.; Xu, Z.; Tan, X.; Wang, H.; Holt, C.M.; Stephenson, T.; Olsen, B.C.; Mitlin, D. Mesoporous nitrogen-rich carbons derived from protein for ultra-high capacity battery anodes and supercapacitors. *Energy Environ. Sci.* **2013**, *6*, 871–878. [CrossRef]
132. Ou, J.; Zhang, Y.; Chen, L.; Zhao, Q.; Meng, Y.; Guo, Y.; Xiao, D. Nitrogen-rich porous carbon derived from biomass as a high performance anode material for lithium ion batteries. *J. Mater. Chem. A* **2015**, *3*, 6534–6541. [CrossRef]
133. Hou, J.; Cao, C.; Idrees, F.; Ma, X. Hierarchical porous nitrogen-doped carbon nanosheets derived from silk for ultrahigh-capacity battery anodes and supercapacitors. *ACS Nano* **2015**, *9*, 2556–2564. [CrossRef]
134. Liu, Y.; Wang, X.; Dong, Y.; Wang, Z.; Zhao, Z.; Qiu, J. Nitrogen-doped graphene nanoribbons for high-performance lithium ion batteries. *J. Mater. Chem. A* **2014**, *2*, 16832–16835. [CrossRef]
135. Tian, L.-L.; Wei, X.-Y.; Zhuang, Q.-C.; Jiang, C.-H.; Wu, C.; Ma, G.-Y.; Zhao, X.; Zong, Z.-M.; Sun, S.-G. Bottom-up synthesis of nitrogen-doped graphene sheets for ultrafast lithium storage. *Nanoscale* **2014**, *6*, 6075–6083. [CrossRef]
136. Wang, S.; Yang, L.; Stubbs, L.; Li, X.; He, C.; Fibrous, L.-D.F.E.C. Mats as High Performance Anode Materials for Lithium Ion Batteries. *ACS Appl. Mater. Interfaces* **2013**, *5*, 12275–12282. [CrossRef]
137. Li, X.; Zhu, X.; Zhu, Y.; Yuan, Z.; Si, L.; Qian, Y. Porous nitrogen-doped carbon vegetable-sponges with enhanced lithium storage performance. *Carbon* **2014**, *69*, 515–524. [CrossRef]
138. Li, D.; Ding, L.-X.; Chen, H.; Wang, S.; Li, Z.; Zhu, M.; Wang, H. Novel nitrogen-rich porous carbon spheres as a high-performance anode material for lithium-ion batteries. *J. Mater. Chem. A* **2014**, *2*, 16617–16622. [CrossRef]
139. Hu, C.; Xiao, Y.; Zhao, Y.; Chen, N.; Zhang, Z.; Cao, M.; Qu, L. Highly nitrogen-doped carbon capsules: Scalable preparation and high-performance applications in fuel cells and lithium ion batteries. *Nanoscale* **2013**, *5*, 2726–2733. [CrossRef] [PubMed]
140. Jia, X.; Zhang, G.; Wang, T.; Zhu, X.; Yang, F.; Li, Y.; Lu, Y.; Wei, F. Monolithic nitrogen-doped graphene frameworks as ultrahigh-rate anodes for lithium ion batteries. *J. Mater. Chem. A* **2015**, *3*, 15738–15744. [CrossRef]
141. Jiang, Y.; Jiang, Z.-J.; Yang, L.; Cheng, S.; Liu, M. A high-performance anode for lithium ion batteries: Fe_3O_4 microspheres encapsulated in hollow graphene shells. *J. Mater. Chem. A* **2015**, *3*, 11847–11856. [CrossRef]
142. He, C.; Wang, R.; Fu, H.; Shen, P.K. Nitrogen-self-doped graphene as a high capacity anode material for lithium-ion batteries. *J. Mater. Chem. A* **2013**, *1*, 14586–14591. [CrossRef]

143. Freunberger, S.A.; Chen, Y.; Peng, Z.; Griffin, J.M.; Hardwick, L.J.; Bardé, F.; Novák, P.; Bruce, P.G. Reactions in the Rechargeable Lithium–O2 Battery with Alkyl Carbonate Electrolytes. *J. Am. Chem. Soc.* **2011**, *133*, 8040–8047. [CrossRef]
144. Lee, J.-S.; Tai Kim, S.; Cao, R.; Choi, N.-S.; Liu, M.; Lee, K.T.; Cho, J. Metal–Air Batteries with High Energy Density: Li–Air versus Zn–Air. *Adv. Energy Mater.* **2011**, *1*, 34–50. [CrossRef]
145. Yang, S.; Knickle, H. Design and analysis of aluminum/air battery system for electric vehicles. *J. Power Sources* **2002**, *112*, 162–173. [CrossRef]
146. Xiong, D.; Li, X.; Bai, Z.; Shan, H.; Fan, L.; Wu, C.; Li, D.; Lu, S. Superior Cathode Performance of Nitrogen-Doped Graphene Frameworks for Lithium Ion Batteries. *ACS Appl. Mater. Interfaces* **2017**, *9*, 10643–10651. [CrossRef] [PubMed]
147. Liu, Z.; Nie, H.; Yang, Z.; Zhang, J.; Jin, Z.; Lu, Y.; Xiao, Z.; Huang, S. Sulfur–nitrogen co-doped three-dimensional carbon foams with hierarchical pore structures as efficient metal-free electrocatalysts for oxygen reduction reactions. *Nanoscale* **2013**, *5*, 3283–3288. [CrossRef] [PubMed]
148. Zhou, X.; Bai, Z.; Wu, M.; Qiao, J.; Chen, Z. 3-Dimensional porous N-doped graphene foam as a non-precious catalyst for the oxygen reduction reaction. *J. Mater. Chem. A* **2015**, *3*, 3343–3350. [CrossRef]
149. Yun, X.; Li, J.; Chen, X.; Chen, H.; Xiao, L.; Xiang, K.; Chen, W.; Liao, H.; Zhu, Y. Porous Fe2O3 Modified by Nitrogen-Doped Carbon Quantum Dots/Reduced Graphene Oxide Composite Aerogel as a High-Capacity and High-Rate Anode Material for Alkaline Aqueous Batteries. *ACS Appl. Mater. Interfaces* **2019**, *11*, 36970–36984. [CrossRef]
150. Yang, J.; Hu, J.; Weng, M.; Tan, R.; Tian, L.; Yang, J.; Amine, J.; Zheng, J.; Chen, H.; Pan, F. Fe-Cluster Pushing Electrons to N-Doped Graphitic Layers with Fe3C(Fe) Hybrid Nanostructure to Enhance O2 Reduction Catalysis of Zn-Air Batteries. *ACS Appl. Mater. Interfaces* **2017**, *9*, 4587–4596. [CrossRef]
151. Zhu, Y.-P.; Ran, J.; Qiao, S.-Z. Scalable Self-Supported Graphene Foam for High-Performance Electrocatalytic Oxygen Evolution. *ACS Appl. Mater. Interfaces* **2017**, *9*, 41980–41987. [CrossRef]
152. Lin, C.; Li, X.; Shinde, S.S.; Kim, D.-H.; Song, X.; Zhang, H.; Lee, J.-H. Long-Life Rechargeable Zn Air Battery Based on Binary Metal Carbide Armored by Nitrogen-Doped Carbon. *ACS Appl. Energy Mater.* **2019**, *2*, 1747–1755. [CrossRef]
153. Yang, H.B.; Miao, J.; Hung, S.-F.; Chen, J.; Tao, H.B.; Wang, X.; Zhang, L.; Chen, R.; Gao, J.; Chen, H.M.; et al. Identification of catalytic sites for oxygen reduction and oxygen evolution in N-doped graphene materials: Development of highly efficient metal-free bifunctional electrocatalyst. *Sci. Adv.* **2016**, *2*, e1501122. [CrossRef]
154. Wang, Z.-D.; Bai, C.-K.; Chen, X.-Y.; Wang, B.-D.; Lu, G.-L.; Sun, H.; Liu, Z.-N.; Huang, H.; Liang, S.; Zang, H.-Y. Co/Co9S8 nanoparticles coupled with N,S-doped graphene-based mixed-dimensional heterostructures as bifunctional electrocatalysts for the overall oxygen electrode. *Inorg. Chem. Front.* **2019**, *6*, 2558–2565. [CrossRef]
155. Qin, X.; Huang, Y.; Wang, K.; Xu, T.; Wang, Y.; Liu, P.; Kang, Y.; Zhang, Y. Novel hierarchically porous Ti-MOFs/nitrogen-doped graphene nanocomposite served as high efficient oxygen reduction reaction catalyst for fuel cells application. *Electrochim. Acta* **2019**, *297*, 805–813. [CrossRef]
156. Wang, Q.; Ji, Y.; Lei, Y.; Wang, Y.; Wang, Y.; Li, Y.; Wang, S. Pyridinic-N-Dominated Doped Defective Graphene as a Superior Oxygen Electrocatalyst for Ultrahigh-Energy-Density Zn–Air Batteries. *ACS Energy Lett.* **2018**, *3*, 1183–1191. [CrossRef]
157. Wen, Z.; Shen, C.; Lu, Y. Air electrode for the lithium–air batteries: Materials and structure designs. *ChemPlusChem* **2015**, *80*, 270–287. [CrossRef]
158. Kunanusont, N.; Shimoyama, Y. Porous carbon electrode for Li-air battery fabricated from solvent expansion during supercritical drying. *J. Supercrit. Fluids* **2018**, *133*, 77–85. [CrossRef]
159. Pan, J.; Xu, Y.Y.; Yang, H.; Dong, Z.; Liu, H.; Xia, B.Y. Advanced Architectures and Relatives of Air Electrodes in Zn–Air Batteries. *Adv. Sci.* **2018**, *5*, 1700691. [CrossRef] [PubMed]